Title

Targeting prostate tumor low—molecular weight tyrosine phosphatase for oxidation-sensitizing therapy

Journal

Science Advances, 10(5)

ISSN

2375-2548

Authors

Stanford, Stephanie M

Nguyen, Tiffany P

Chang, Joseph

et al.

Publication Date

2024-02-02

DOI

10.1126/sciadv.adg7887

CANCER

Targeting prostate tumor low–molecular weight tyrosine phosphatase for oxidation-sensitizing therapy

Stephanie M. Stanford[1]†, Tiffany P. Nguyen[1]†, Joseph Chang[1], Zixuan Zhao[1], G. Lavender Hackman[2], Eugenio Santelli[1,3], Colton M. Sanders[1], Madhusudhanarao Katiki[4], Eleonora Dondossola[5], Brooke L. Brauer[6,7], Michael A. Diaz[1], Yuan Zhan[13], Sterling H. Ramsey[1], Philip A. Watson[8], Banumathi Sankaran[9], Claudia Paindelli[5], Vanessa Parietti[5], Antonios G. Mikos[10], Alessia Lodi[2], Aditya Bagrodia[11], Andrew Elliott[12], Rana R. McKay[1], Ramachandran Murali[4], Stefano Tiziani[2,13], Arminja N. Kettenbach[6,7], Nunzio Bottini[1,3]*

Protein tyrosine phosphatases (PTPs) play major roles in cancer and are emerging as therapeutic targets. Recent reports suggest low–molecular weight PTP (LMPTP)—encoded by the *ACP1* gene—is overexpressed in prostate tumors. We found *ACP1* up-regulated in human prostate tumors and *ACP1* expression inversely correlated with overall survival. Using CRISPR-Cas9–generated LMPTP knockout C4-2B and MyC-CaP cells, we identified LMPTP as a critical promoter of prostate cancer (PCa) growth and bone metastasis. Through metabolomics, we found that LMPTP promotes PCa cell glutathione synthesis by dephosphorylating glutathione synthetase on inhibitory Tyr^{270}. PCa cells lacking LMPTP showed reduced glutathione, enhanced activation of eukaryotic initiation factor 2–mediated stress response, and enhanced reactive oxygen species after exposure to taxane drugs. LMPTP inhibition slowed primary and bone metastatic prostate tumor growth in mice. These findings reveal a role for LMPTP as a critical promoter of PCa growth and metastasis and validate LMPTP inhibition as a therapeutic strategy for treating PCa through sensitization to oxidative stress.

INTRODUCTION

Prostate cancer (PCa) is the most common cancer and second leading cause of cancer death in American men (*1*, *2*). Many patients develop advanced PCa, for which the main treatment is androgen deprivation therapy (*3*). Unfortunately, a subset of patients develop metastatic castration-resistant disease, which is universally fatal. The most common sites of metastasis include the lymph nodes and bone, followed by the development of visceral metastases to the lung and liver (*4*, *5*). Novel therapies to inhibit primary and metastatic PCa tumor growth are a major unmet medical need in improving outcomes for patients with PCa.

Protein tyrosine phosphatases (PTPs) play major roles in cancer growth and metastasis and are emerging as targets for anti-cancer agents (*6*). The low–molecular weight PTP (LMPTP) is a ubiquitously expressed PTP encoded by the *ACP1* gene (*7*–*9*). LMPTP belongs to the structurally unique class 2 cysteine-based PTPs, which show homology to some bacterial arsenate reductases and consist only of LMPTP and the recently reclassified suppressor of Sua7-2 (SSu72) (*10*, *11*). LMPTP is considered an inhibitor of receptor tyrosine kinases (RTKs) such as the insulin receptor (IR) through dephosphorylation of phospho-tyrosine residues in the kinase activation motif (*12*, *13*). In the liver, LMPTP promotes obesity-induced insulin resistance through negative regulation of the IR (*14*, *15*). LMPTP also promotes adipogenesis through inhibition of basal platelet-derived growth factor receptor α tyrosine phosphorylation in pre-adipocytes and obesity-induced subcutaneous adipocyte hypertrophy (*16*).

Recent reports have emerged, suggesting that *ACP1* is up-regulated in certain cancers (*17*–*22*). *ACP1* expression was reported to be increased in primary prostate tumor tissue and metastatic lesions. These reports suggest high *ACP1* expression correlates with post-surgical biochemical and local recurrence and inversely correlates with patient survival time in metastatic PCa (*17*–*19*). *ACP1* is also reported to be up-regulated in human colorectal cancer (CRC) tumors (*20*–*22*) and colon tumors in rat models (*23*, *24*). Transient overexpression of LMPTP in cancer cell lines enhances their migration in vitro (*18*) and LMPTP knockdown decreases CRC cell migration (*20*). These intriguing reports suggest a potential oncogenic role for LMPTP; however, its mechanism of action is largely unknown. We thus decided to investigate a potential pathogenic role for LMPTP in PCa.

RESULTS

ACP1 expression is increased in prostate tumor tissue and negatively correlates with patient prognosis

We examined *ACP1* expression in prostate adenocarcinoma (PRAD) patient samples from The Cancer Genome Atlas (TCGA). Using the

[1]Department of Medicine, University of California, San Diego, La Jolla, CA, USA. [2]Department of Nutritional Sciences, College of Natural Sciences and Department of Pediatrics, Dell Medical School, The University of Texas at Austin, Austin, TX, USA. [3]Kao Autoimmunity Institute, Cedars-Sinai Medical Center, Los Angeles, CA, USA. [4]Department of Biomedical Sciences, Cedars-Sinai Medical Center, Los Angeles, CA, USA. [5]Department of Genitourinary Medical Oncology and David H. Koch Center for Applied Research of Genitourinary Cancers, The University of Texas MD Anderson Cancer Center, Houston, TX, USA. [6]Department of Biochemistry and Cell Biology, Geisel School of Medicine at Dartmouth, Hanover, NH, USA. [7]Norris Cotton Cancer Center, Geisel School of Medicine at Dartmouth, Lebanon, NH, USA. [8]Human Oncology and Pathogenesis Program, Memorial Sloan Kettering Cancer Center, New York, NY, USA. [9]Department of Molecular Biophysics and Integrated Bioimaging, Berkeley Center for Structural Biology, Lawrence Berkeley National Laboratory, Berkeley, CA, USA. [10]Department of Bioengineering, Rice University, Houston, TX, USA. [11]Department of Urology, University of California, San Diego, La Jolla, CA, USA. [12]Department of Clinical and Translational Research, Caris Life Sciences, Phoenix, AZ, USA. [13]Department of Pediatrics and Department of Oncology, Dell Medical School, Livestrong Cancer Institutes, College of Natural Sciences, The University of Texas at Austin, Austin, TX USA.
*Corresponding author. Email: nunzio.bottini@cshs.org
†These authors contributed equally to this work.

University of ALabama at Birmingham CANcer data analysis (UALCAN) interface, we found that *ACP1* expression is significantly increased in prostate tumor tissue compared to normal, noncancerous prostate tissue (Fig. 1A). Stratification of samples by tumor Gleason score revealed significantly higher *ACP1* expression in tumors with high Gleason scores (8 or 9) compared to tumors with low (6) or intermediate (7) Gleason scores (Fig. 1B) (*25*). *ACP1* expression was also significantly increased in primary tumors of patients with lymph node metastasis compared to patients without nodal metastasis (Fig. 1C). Similarly, analysis of *ACP1* expression in a commercial next-generation sequencing (NGS) (Caris Life Sciences) cohort of patients with PCa also demonstrated significantly higher *ACP1* expression in lymph nodes and metastatic sites versus primary prostate tumors (Fig. 1D). Concordantly, in a comparison of basal, luminal A and luminal B PCa subtypes (*26*) using the Prostate Cancer Transcriptome Atlas, *ACP1* expression was significantly higher in the more aggressive luminal B PCa subtype (fig. S1). We also examined expression of *ACP1* mRNA by quantitative polymerase chain reaction (qPCR) and LMPTP protein by Western blotting in matched prostatectomy tumor versus nontumor tissue obtained from the Prostate Cancer Biorepository Network (PCBN) and confirmed significantly higher *ACP1* expression at the mRNA (Fig. 1E) and protein levels in tumor versus nontumor tissue (Fig. 1F).

High expression of *ACP1*, defined as patients within the upper quartile of PRAD *ACP1* expression in the TCGA and commercial NGS cohorts, correlated with lower survival probability over a span of greater than 10 years (Fig. 1, G and H). To compare the effect of *ACP1* expression on survival probability of patients with similar cancer stage, we examined the last known survival status of T3 stage PRAD patients in TCGA using the University of California Santa Cruz (UCSC) Xena browser. High *ACP1* expression, defined as within the upper tercile, correlated with substantially lower survival probability for T3 stage PCa, with <50% survival for patients with high *ACP1* expression at 7.5 years but 100% survival in patients with low/medium *ACP1* expression at 10 years (Fig. 1I). Together, these data suggest that LMPTP is up-regulated in prostate tumors, and its expression is associated with more aggressive cancer and a worse prognosis.

LMPTP promotes PCa growth in vitro and in vivo

To study the role of LMPTP in PCa, we generated LMPTP knockout (KO) MyC-CaP and C4-2B cell clones via CRISPR-Cas9 (figs. S2 and S3). We first tested the effect of LMPTP KO on cell growth. As shown in Fig. 2 (A and B), loss of LMPTP substantially reduced the growth of both MyC-CaP and C4-2B LMPTP KO cells.

Next, we assessed the proliferative effects of LMPTP using a subcutaneous prostate tumor xenograft model. We inoculated severe combined immunodeficiency disease (SCID) mice with wild-type (WT) and LMPTP KO MyC-CaP cells and monitored tumor growth. LMPTP KO tumor volumes were notably smaller, and mice carrying LMPTP KO tumors displayed significantly longer times to reach the tumor size end point (Fig. 2, C and D). To determine whether the tumor-promoting action of LMPTP is dependent on its phosphatase activity, we used a highly selective chemical inhibitor of LMPTP, compound (Compd.) 23, which our laboratory previously found and used to investigate the role of LMPTP in diet-induced obesity (*14*). We previously showed that Compd. 23 is orally bioavailable and inhibits LMPTP through an uncompetitive mechanism that confers exquisite selectivity to LMPTP over other tyrosine phosphatases (*14*). SCID mice with MyC-CaP tumors were placed on regular chow or chow formulated with 0.1% (w/w) Compd. 23, a dose expected to maintain inhibitor levels above the ~800 nM median inhibitory concentration (*14*). Mice treated with Compd. 23 displayed significantly reduced tumor growth, without displaying weight loss (Fig. 2, E and F). LMPTP KO also substantially reduced the growth of C4-2B cells in a subcutaneous tumor xenograft model and extended the time to reach the tumor size endpoint (Fig. 2, G and H). Together, these data suggest that LMPTP is a critical promoter of prostate tumor growth through its catalytic activity.

LMPTP promotes PCa invasiveness and tumorigenesis

Because survival probability among patients with PCa is substantially reduced once tumor metastasis occurs (*27*), we assessed whether LMPTP affects the metastatic potential of prostate tumor cells. We first examined the effect of LMPTP deletion on PCa cell invasiveness using a transwell assay in which cells are allowed to invade through an extracellular matrix. As shown in Fig. 3 (A and B), LMPTP KO in both MyC-CaP and C4-2B cells significantly impaired their ability to invade through Matrigel. Similarly, treatment with LMPTP inhibitor Compd. 23 also significantly reduced the invasiveness of MyC-CaP and C4-2B cells (Fig. 3, C and D), suggesting that the pro-invasive role of LMPTP is activity dependent. We next explored the effects of LMPTP deletion on the ability of PCa cells to form new, anchorage-independent tumors. As shown in Fig. 3 (E and F), LMPTP KO MyC-CaP and C4-2B cells displayed significantly impaired ability to form colonies when plated in soft agar. Together, these results suggest that LMPTP promotes both PCa cell invasiveness and tumorigenesis, key features needed for formation of metastatic PCa tumors.

LMPTP promotes PCa bone metastasis

Bone metastasis is a highly lethal form of metastatic PCa (*28*). To explore whether LMPTP is important for the ability of prostate tumor cells to metastasize into bone, we used an established three-dimensional (3D) in vitro bone mimetic environment (BME) (*29*–*31*). This system consists of human mesenchymal stem cells seeded onto 3D polycaprolactone (PCL) scaffolds exposed to osteogenic stimuli for 30 days to induce osteoblastic differentiation (scheme shown in Fig. 3G); thus, we used the human C4-2B cell line. When WT and LMPTP KO C4-2B cells were formed as spheroids and seeded on the 3D BMEs, the LMPTP KO cells displayed substantially reduced growth compared to the WT cells (Fig. 3H). Similarly, treatment with LMPTP inhibitor Compd. 23 significantly impaired growth of WT C4-2B spheroids in the 3D BME (Fig. 3I).

We next assessed the effects of LMPTP deletion on prostate tumor growth in bone using an intraosseous mouse model. Using CRISPR-Cas9 technology, we deleted LMPTP in luciferase-expressing MyC-CaP cells (MyC-CaP/GFP-Luc; fig. S4). SCID mice were inoculated intratibially with WT and LMPTP KO MyC-CaP/GFP-Luc cells, and tumor growth was monitored by luciferase-generated luminescence upon in vivo administration of luciferin. LMPTP deletion considerably reduced intraosseous growth of MyC-CaP/GFP-Luc tumors (Fig. 3J). Administration of LMPTP inhibitor Compd. 23 also substantially reduced the growth of intraosseous MyC-CaP/GFP-Luc tumors (Fig. 3K). These findings suggest that LMPTP is a key promoter of prostate tumor metastasis into bone and LMPTP inhibition impairs the growth of these tumors in vivo.

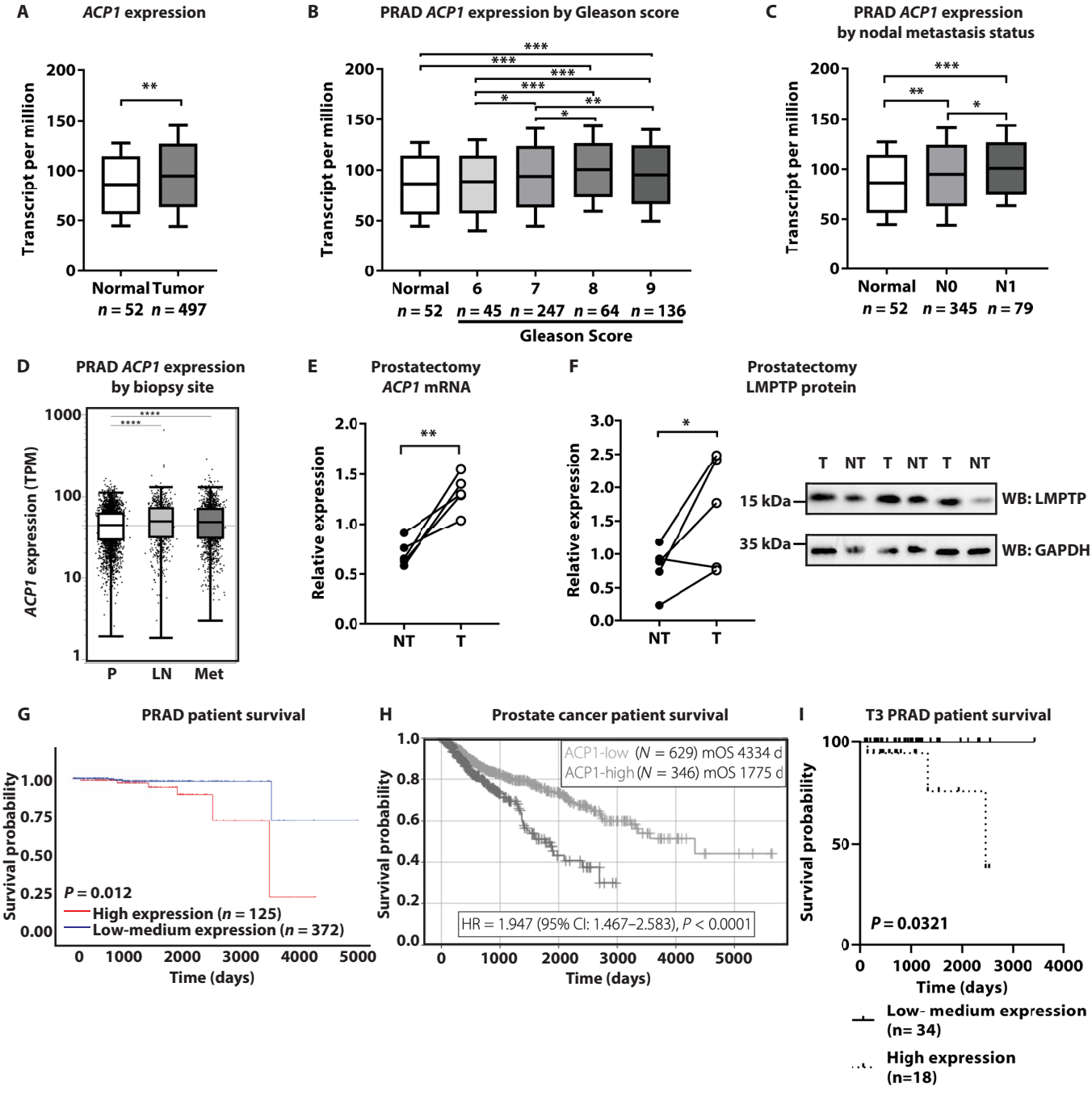

Fig. 1. *ACP1* is up-regulated in prostate tumors and correlates negatively with patient survival. (**A** to **C**) *ACP1* expression in PRAD from TCGA, processed through UALCAN. *ACP1* mRNA in normal and primary prostate tumor tissue. Expression was subclassified by (B) Gleason score and (C) metastasis status (N0 = no lymph node metastasis; N1 = metastases in one to three lymph nodes). Boxes: median, lower, and upper quartiles; whiskers: range of minimum to maximum. Significance reported in UALCAN: *$P < 0.05$, **$P < 0.01$, and ***$P < 0.001$, *t* test. (**D**) *ACP1* mRNA in PCa patient samples from the Caris Life Sciences cohort stratified by primary (prostate, P), lymph node (LN), and metastatic (Met) biopsy sites. TPM, transcripts per million. Boxes: median, lower, and upper quartiles; whiskers: range of minimum to maximum, excluding statistical outliers (1.5× the inner quartile range). ****$P < 0.0001$, Mann-Whitney *U* test. (**E** and **F**) *ACP1* mRNA assessed by qPCR (E) and LMPTP protein assessed by Western blotting (WB) using mouse anti-LMPTP antibody (F) from five paired tumor/nontumor PCBN prostatectomy samples with Gleason score 8/9. Means ± SEM expression relative to *POLR2A* (E) or glyceraldehyde 3-phosphate dehydrogenase (GAPDH) (F) is shown. Representative blots (F). *$P < 0.05$ and **$P < 0.01$, paired *t* test. (**G**) Survival probability of patients with low/medium or high (upper quartile) *ACP1* expression from TCGA. Significance was reported in UALCAN using log-rank test. (**H**) Overall patient survival measured from time of tumor biopsy for samples with low or high *ACP1* (<25th and >75th percentiles of overall cohort) from Caris Life Sciences cohort. Survival curves were compared using log-rank test and hazard ratios (HRs) with 95% confidence interval (CI) estimated by Cox proportional hazards model. mOS, median overall survival; d, days. (**I**) Survival probability of T3 stage patients with low/medium or high (upper tercile) *ACP1* expression from TCGA, processed through UCSC Xena. Ticks denote last known survival status. Significance calculated by log-rank test.

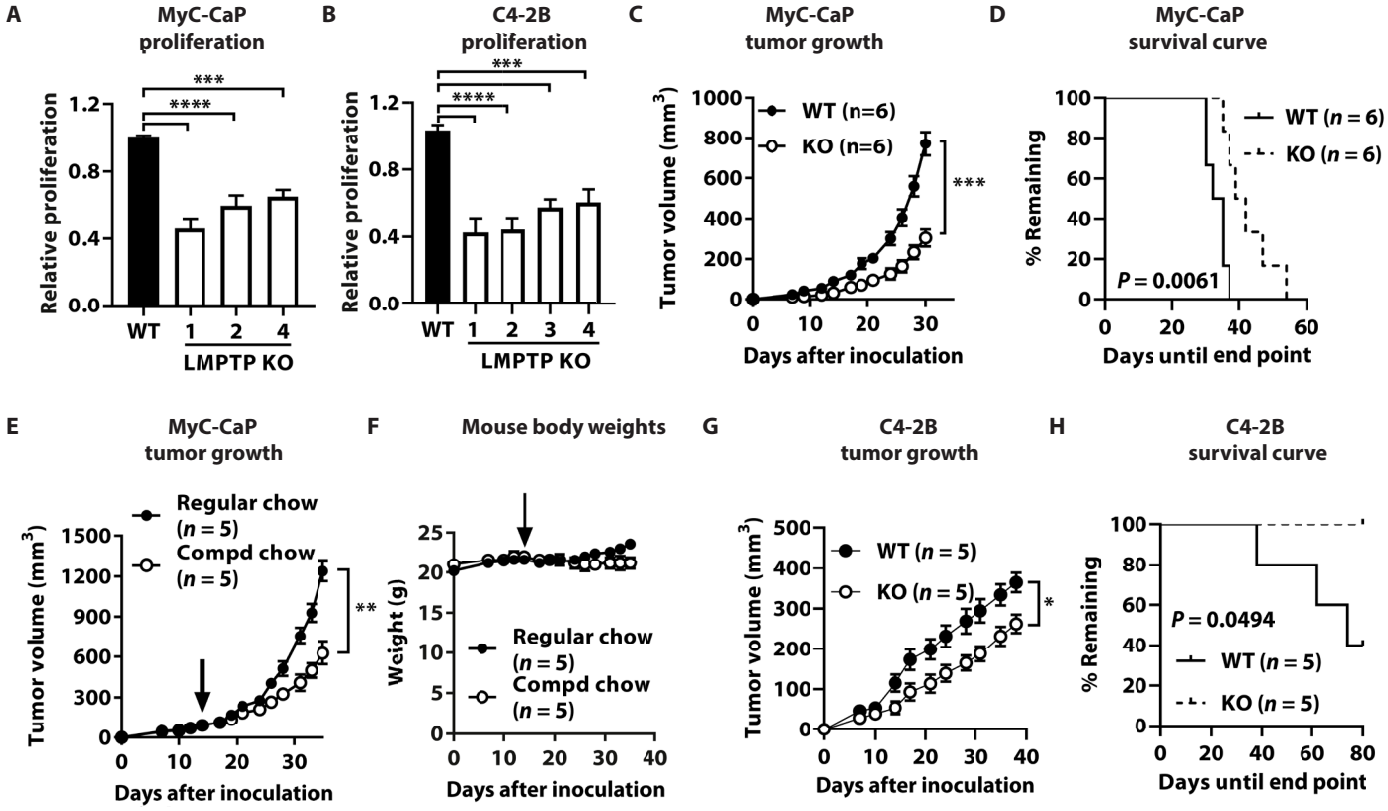

Fig. 2. Loss of LMPTP impairs PCa cell growth. (**A** and **B**) WT and LMPTP KO MyC-CaP (A) and C4-2B (B) cells were plated and allowed to grow. After 5 days, cells were fixed and stained with crystal violet. Stain was extracted and quantified by absorbance at 590 nM. Mean ± SEM proliferation relative to WT samples (MyC-CaP: $n = 5$ per WT and $n = 4$ per KO line; C4-2B: $n = 5$ per WT/KO line) is shown. (**C** to **H**) SCID mice were injected subcutaneously with MyC-CaP or C4-2B cells suspended in Matrigel. (C) and (G) Tumor volumes of mice inoculated with WT or LMPTP KO MyC-CaP (C) or C4-2B (G) cells were measured with a caliper at the indicated time points. Mean ± SEM tumor volume is shown. (D) and (H) Kaplan-Meier survival plot of mice from [(C) and (G)]. The experimental endpoint was determined when tumors reached 1.5–2 cm long. Significance was determined using the log-rank test. (E) to (F) 14 days after inoculation with WT MyC-CaP cells, mice were placed on regular chow or chow formulated with 0.1% (w/w) LMPTP inhibitor Compd. 23 (black arrow indicates start of treatment). (E) Mean ± SEM tumor volume is shown. (F) Mean ± SEM mouse body weight is shown. $^*P < 0.05$, $^{**}P < 0.01$, $^{***}P < 0.001$, and $^{****}P < 0.0001$, one-way analysis of variance (ANOVA) with Dunnett's correction (A and B) and two-way ANOVA [(C), (E), and (G)].

Metabolomics reveals LMPTP as a key promoter of glutathione synthesis

To gain insight into the mechanism underlying the role of LMPTP in PCa cell function(s), we used metabolomics to explore alterations occurring in PCa cells lacking LMPTP. We performed ultrahigh-performance liquid chromatography–mass spectrometry (UHPLC-MS)–based analysis of the intracellular metabolomes of WT and LMPTP KO MyC-CaP and C4-2B cells. Principal components analysis (PCA) revealed clear separation between WT and LMPTP KO cells of each line (Fig. 4, A and B). Volcano plots for each line revealed metabolites exhibiting the greatest significance and fold change between WT and LMPTP KO cells (Fig. 4, C and D). Among those appreciably affected in both LMPTP KO cell lines were metabolic intermediates of the glutathione synthesis pathway. Glutathione is a tripeptide composed of glutamate, cysteine, and glycine (*32*, *33*). Glutamine and cystine both enter the cell through transporters and are converted to glutamate and cysteine, respectively. Glycine is synthesized through multiple pathways from amino acid precursors and present at high abundance in cells. Glutathione is synthesized in a two-step process (Fig. 4E). In the first step, which is rate limiting, γ-glutamylcysteine is formed from glutamate and cysteine by the glutamate cysteine ligase enzyme. In the second step, glutathione is formed by the addition of glycine to γ-glutamylcysteine by the adenosine triphosphate (ATP)–dependent glutathione synthetase (GSS) enzyme. In both LMPTP KO cell types, we noticed substantial increases in γ-glutamylcysteine precursors glutamine and cystine (Fig. 4, F and G). Glutamate levels were significantly lower in LMPTP KO cells (Fig. 4, F and G), while cysteine was not detected. In LMPTP KO MyC-CaP, GSS substrate γ-glutamylcysteine was significantly increased (Fig. 4F). Unexpectedly, however, glutathione levels were notably decreased in LMPTP KO MyC-CaP (Fig. 4F). While in all C4-2B cells, the levels of γ-glutamylcysteine and glutathione were barely detectable, we did detect significantly increased levels of γ-glutamylcysteine derivative 5-oxoproline in LMPTP KO compared to WT C4-2B (Fig. 4G). Because the metabolomic data suggested alterations in the glutathione synthesis pathway in LMPTP KO cells, we tested the intracellular levels of total glutathione, oxidized glutathione (GSSG), and reduced glutathione (GSH) using a luminescence-based assay. As shown in Fig. 4 (H to K) and fig. S5, LMPTP deletion in both MyC-CaP and C4-2B cells led to significantly reduced levels of all forms of glutathione. Glutathione levels were also reduced in MyC-CaP and C4-2B cells treated with

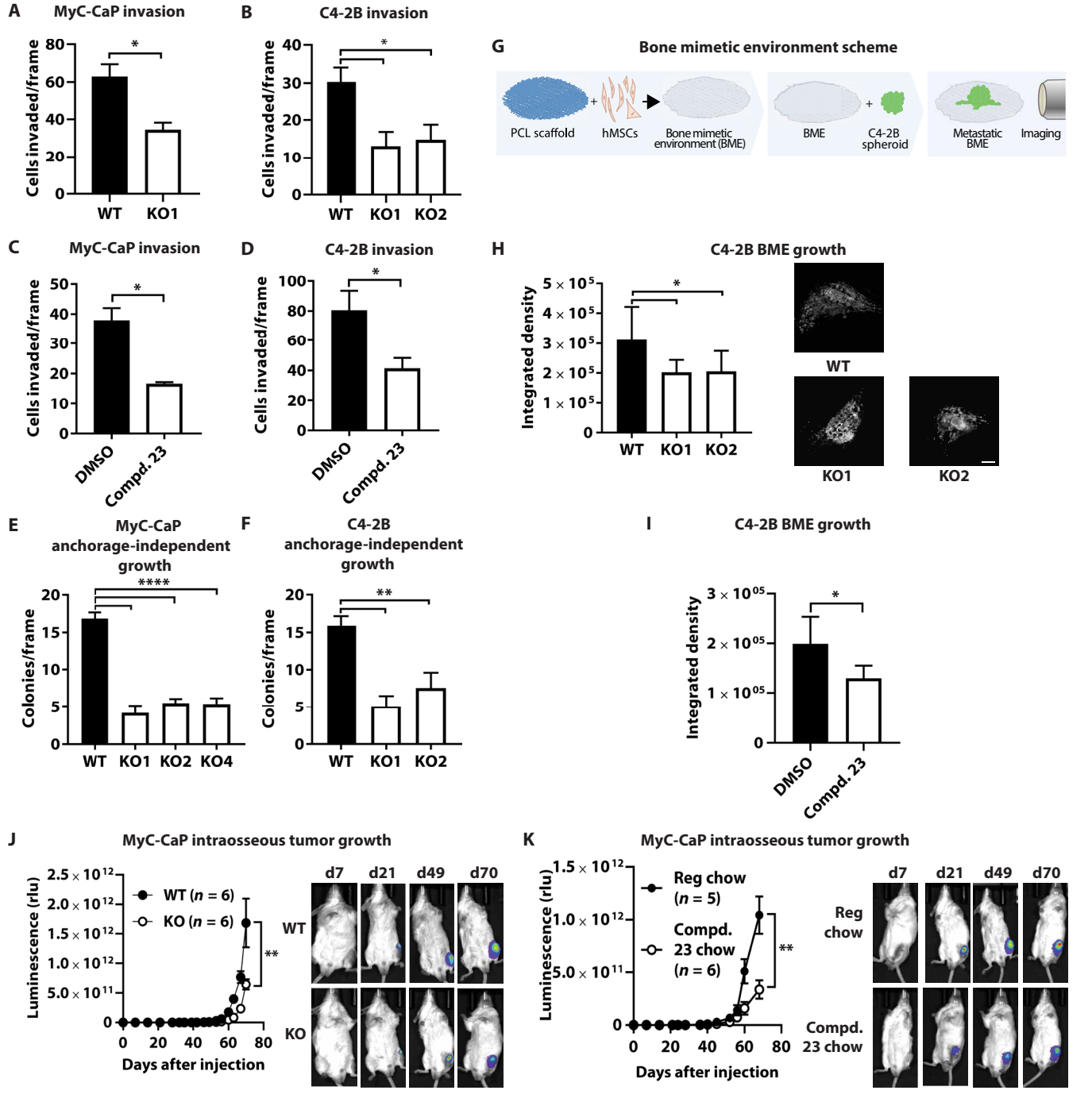

Fig. 3. LMPTP KO impairs metastatic features of PCa. (**A** and **B**) WT or LMPTP KO MyC-CaP (A) and C4-2B (B) cell invasion through Matrigel-coated transwells. Mean ± SEM number of invaded cells/frame from four (A) or six (B) independent experiments with three transwells each. (**C** and **D**) MyC-CaP (C) and C4-2B (D) cell invasion as in (A) and (B) in the presence of 10 μM LMPTP inhibitor Compd. 23 or dimethyl sulfoxide (DMSO). Mean ± SEM number of invaded cells/frame from four independent experiments with three transwells each. (**E** and **F**) Colony formation of WT or LMPTP KO MyC-CaP (E) and C4-2B (F) colonies 21 days after seeding on noble agar. Mean ± SEM number of colonies formed/frame (MyC-CaP: $n = 4$/line; C4-2B: $n = 4$ for WT/KO1; $n = 3$ for KO2). (**G**) Schematic of the BME assay. Human mesenchymal stem cells (hMSCs) were seeded on polycaprolactone (PCL) scaffolds and maintained in osteogenic medium. (**H**) WT and LMPTP KO C4-2B were seeded on the BME as spheroids and monitored by confocal microscopy 10 days after seeding. Left: Mean ± SEM spheroid size measured by fluorescence intensity. Right: Representative spheroids. Bar, 500 μm. (**I**) Size of C4-2B spheroids grown in the presence of 10 μM Compd. 23 or DMSO as assessed by confocal microscopy 10 days after seeding on the BME. (**J** and **K**) Bone tumor growth assay. Luciferase-expressing MyC-CaP were injected into SCID mice tibias. Tumors were monitored for 10 weeks by luminescence imaging. Left: Mean ± SEM luminescent intensity. Right: Representative images. (J) WT and LMPTP KO MyC-CaP. (K) Mice were administered 0.1% (w/w) Compd. 23 in chow or chow alone. $^{*}P < 0.05$, $^{**}P < 0.01$, and $^{****}P < 0.0001$, Mann-Whitney *U* test [(A), (C), (D), and (I)], one-way ANOVA with Dunnett's correction [(B), (E), (F), and (H)], and two-way ANOVA [(J) and (K)]. rlu, relative light unit.

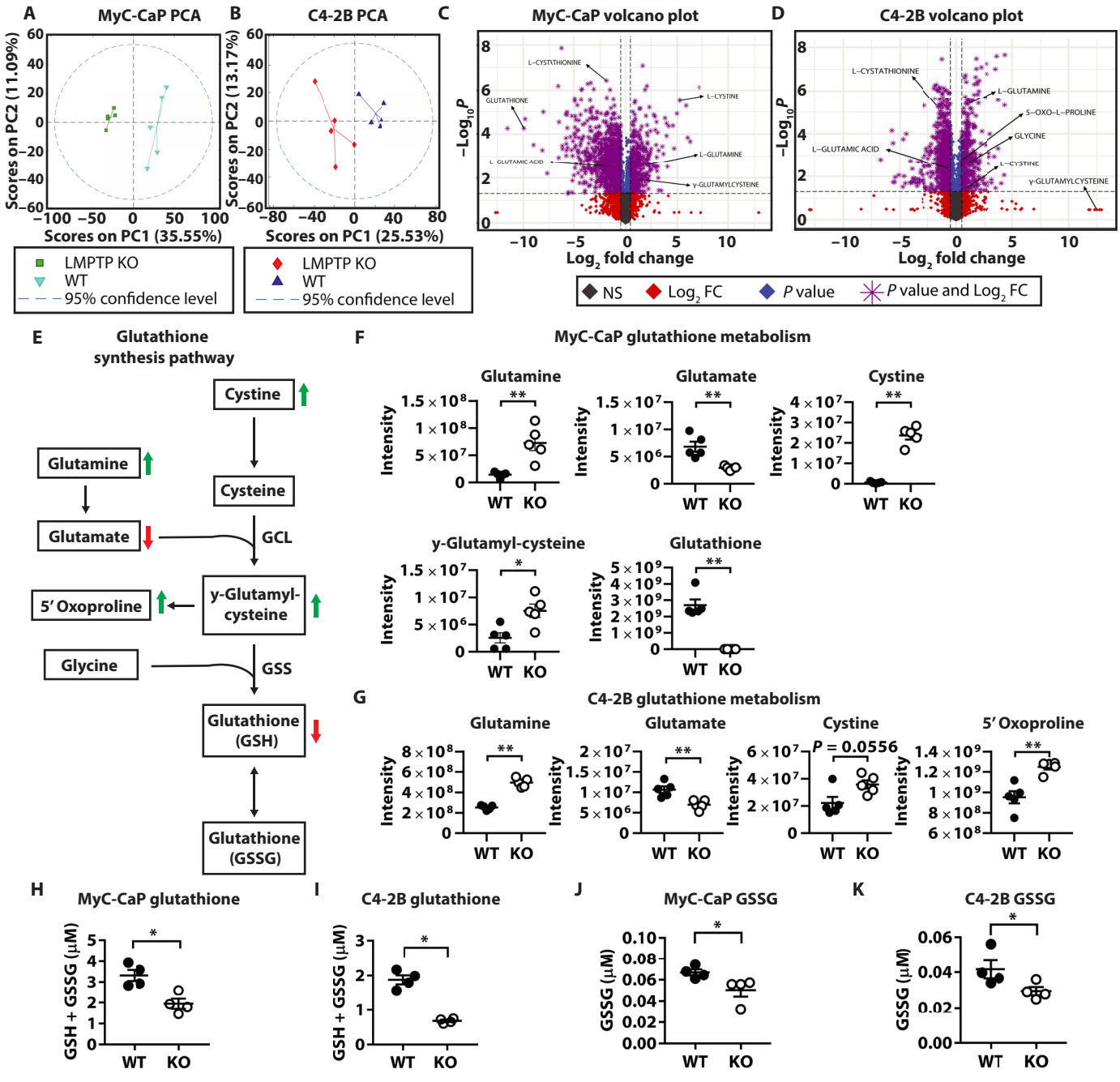

Fig. 4. LMPTP is a key promoter of glutathione synthesis in PCa cells. (**A** to **D** and **F** and **G**) WT and LMPTP KO MyC-CaP [(A), (C), and (F)] and C4-2B [(B), (D), and (G)] cells (five biological replicates per cell clone) were grown overnight, collected, and metabolomes were analyzed by UHPLC-MS. (A) and (B) PCA (PC1 versus PC2) of WT and LMPTP KO MyC-CaP (A) and C4-2B (B) cell metabolomes. (**C** and **D**) Volcano plot comparison of features from metabolomic analyses between WT and LMPTP KO MyC-CaP (C) and C4-2B (D) cells. Fold change cutoff, 1.5; *q* value (false discovery rate corrected *P* value) cutoff, less than 0.05. (**E**) Scheme of glutathione synthesis pathway. Arrows indicate metabolites increased (green upward arrow) or decreased (red downward arrow) in LMPTP KO cells. (**F** and **G**) Intracellular metabolite levels of WT and LMPTP KO MyC-CaP (F) and C4-2B (G) cells within the glutathione synthesis pathway. Mean ± SEM metabolite intensity is shown. (**H** to **K**) Intracellular concentrations of glutathione in WT and LMPTP KO MyC-CaP [(H) and (J)] and C4-2B [(I) and (K)] cells were detected using a bioluminescent glutathione detection assay. Mean ± SEM concentrations of total glutathione [(H) and (I)] and oxidized glutathione (GSSG) [(J) and (K)] from four independent experiments are shown. $^{*}P < 0.05$ and $^{**}P < 0.01$, Mann-Whitney test [(F) to (K)].

LMPTP inhibitor Compd. 23 (fig. S5). Together, these data suggest that LMPTP is a key promoter of glutathione production in PCa cells.

We next examined the mechanism underlying the alterations in glutathione production in PCa cells lacking LMPTP. LMPTP KO MyC-CaP showed excessive levels of the immediate glutathione precursor γ-glutamylcysteine, and loss of LMPTP did not affect levels of glycine in either MyC-CaP or C4-2B (fig. S6), suggesting the block in glutathione production occurred following γ-glutamylcysteine synthesis. Although γ-glutamylcysteine levels could not be detected in C4-2B cells, the excessive 5-oxoproline again suggested a defect downstream of γ-glutamylcysteine production. We thus reasoned there might be a defect in expression or function of the GSS enzyme in cells lacking LMPTP. We tested the expression levels of GSS mRNA and protein in WT and LMPTP KO MyC-CaP and C4-2B cells. As shown in fig. S6, we did not observe any decrease in expression of this enzyme in LMPTP KO cells; in fact, we observed trends toward the opposite. On the basis of these data, we concluded that GSS activity may be defective in PCa cells lacking LMPTP expression. Because LMPTP is a tyrosine phosphatase enzyme, we reasoned that LMPTP may act as a promoter of GSS activity by dephosphorylating GSS on tyrosine residues. We therefore sought to explore if GSS is regulated by phosphorylation on Tyr.

GSS Tyr phosphorylation is enhanced in LMPTP KO PCa cells

To determine whether GSS can be phosphorylated in PCa cells, we overexpressed Flag-tagged GSS in C4-2B cells and treated them with pervanadate, an irreversible PTP inhibitor. GSS Tyr phosphorylation was monitored by Western blotting of anti-Flag immunoprecipitates using anti–phospho-Tyr (pTyr) antibody. As shown in Fig. 5A, the anti-pTyr antibody reacted against immunoprecipitated GSS and significantly more so in cells treated with pervanadate. These results suggest that GSS can be phosphorylated on Tyr residues in PCa cells. We next assessed the effect of LMPTP deletion on GSS Tyr phosphorylation in PCa cells. We observed enhanced Tyr phosphorylation of Flag-GSS overexpressed in LMPTP KO C4-2B and MyC-CaP cells compared to WT C4-2B and MyC-CaP cells, respectively (Fig. 5B and fig. S7). Performing immunoprecipitations with anti-pTyr antibody led to enhanced precipitation of Flag-GSS from LMPTP KO compared to WT C4-2B cell lysates (fig. S7).

Surface plasmon resonance (SPR) reveals binding between LMPTP and GSS

SPR was used to verify binding of GSS to LMPTP recombinant proteins by OneStep binding method using the Taylor dispersion SPR technique (*34, 35*). We measured binding of the LMPTP protein and, as a negative control, an unrelated DNA-binding protein (a transcription factor from the high mobility group box [HMG]-box proteins family) to immobilized GSS protein. The OneStep binding kinetics data were acquired for the LMPTP and HMG-box protein (Fig. 5C). While LMPTP shows 1:1 binding, HMG-box protein shows 1:2 binding presumably due to the small size of HMG-box protein (molecular weight ~ 9 kDa). LMPTP binds to GSS with a dissociation constant (K_D) value of 244 ± 2 nM. The negative control protein, HMG-box protein, shows much weaker binding (K_D values: 180.6 ± 0.7 μM for site 1 and 40 ± 70 mM for site 2), suggesting that GSS binding is more specific to LMPTP.

LMPTP inhibits GSS-Tyr^{270} phosphorylation in PCa cells

We next sought to identify the GSS phosphorylation site under control of LMPTP in PCa cells. A search of the PhosphoSite database revealed Tyr^{270} as a candidate residue for phosphorylation (fig. S7). We thus examined phosphorylation of WT and Tyr^{270}Phe mutant GSS in WT and LMPTP KO PCa cells. As shown in Fig. 5D, mutation of Tyr^{270} abolished the difference in Tyr phosphorylation between WT and LMPTP KO C4-2B cells.

GSS-Tyr^{270} phosphorylation impairs GSS enzymatic activity

We next examined the potential impact of Tyr^{270} phosphorylation on GSS enzymatic activity. Using a luciferase reporter–based assay to detect ATP usage, we measured recombinant GSS-catalyzed glutathione production in vitro from γ-glutamylcysteine and glycine in the presence of ATP. As shown in Fig. 5E, mutation of GSS-Tyr^{270} to Glu to mimic Tyr phosphorylation of this residue markedly reduced GSS enzymatic activity, while the Tyr^{270}Phe mutation had no significant effect on GSS activity. In the crystal structure of human GSS solved in the presence of glutathione and ADP [Protein Data Bank (PDB) code 2HGS], Tyr^{270} is part of a substrate-interacting loop named L2 (residues 266 to 276), with its aromatic ring making multiple hydrophobic contacts at ~3.5 Å from the GSH γ-glutamylcysteinyl group, protecting cysteine from oxidation (*36*). How phosphorylation of Tyr^{270} would affect catalytic activity is, however, not immediately clear from analysis of the structure. We therefore crystallized the Tyr^{270}Glu mutant in the absence of substrates or catalytic products and solved its structure by molecular replacement. As shown in fig. S8, the two structures are globally very similar with root mean square differences of less than 1.0 Å for all Cα atoms. The main differences are a 4- to 5-Å displacement of the N-terminal α helix, likely due to crystal contacts, and, most notably, weak or broken electron density (ED) for two of the loops (residues 366 to 372 and 454 to 466, L3 and L4, respectively) that line the substrate-binding pocket, indicating loss of stable conformation for these residues. Other than the Tyr to Glu substitution, no major differences are observed in the L2 loop despite the absence of the bound glutathione. Three sulfate ions from the crystallization buffer were tentatively modeled in the ED for each monomer despite somewhat asymmetric density possibly indicating mixed occupancy (fig. S8). Two of these ions located in the substrate binding pocket closely overlap with the glutathione-binding site (Fig. 5F); one of the sulfate ions makes 2.6- to 2.9-Å hydrogen bonds to the side chains of Ser^{149}, Asn^{216}, Gln^{220}, and Arg^{267}, while another only forms a short bond to Ser^{151} but is positioned in a highly positively charged region of the pocket. Despite 4.8- and 7.1-Å distances between the sulfur atoms and the Tyr^{270} hydroxyl group in the superposed structure of glutathione-bound GSS, this could provide a clue to the structural basis for the suppression of catalytic activity, as rearrangement of the 266 to 276 loop upon Tyr^{270} phosphorylation could bring the phosphate group to bind to the same sites and sterically hinder γ-glutamylcysteine binding (Fig. 5F).

We next assessed whether abolishing phosphorylation of this site would enhance glutathione production in PCa cells. We overexpressed WT GSS or Tyr^{270}Phe mutated GSS in MyC-CaP and C4-2B cells. As expected, overexpression of WT GSS led to an increase in glutathione production in both cell types, while overexpression of the Tyr^{270}Phe mutant markedly enhanced glutathione production (Fig. 5, G and H). We also observed that LMPTP KO MyC-CaP and C4-2B cells overexpressing phospho-tyrosine mimetic GSS-Tyr^{270}Glu

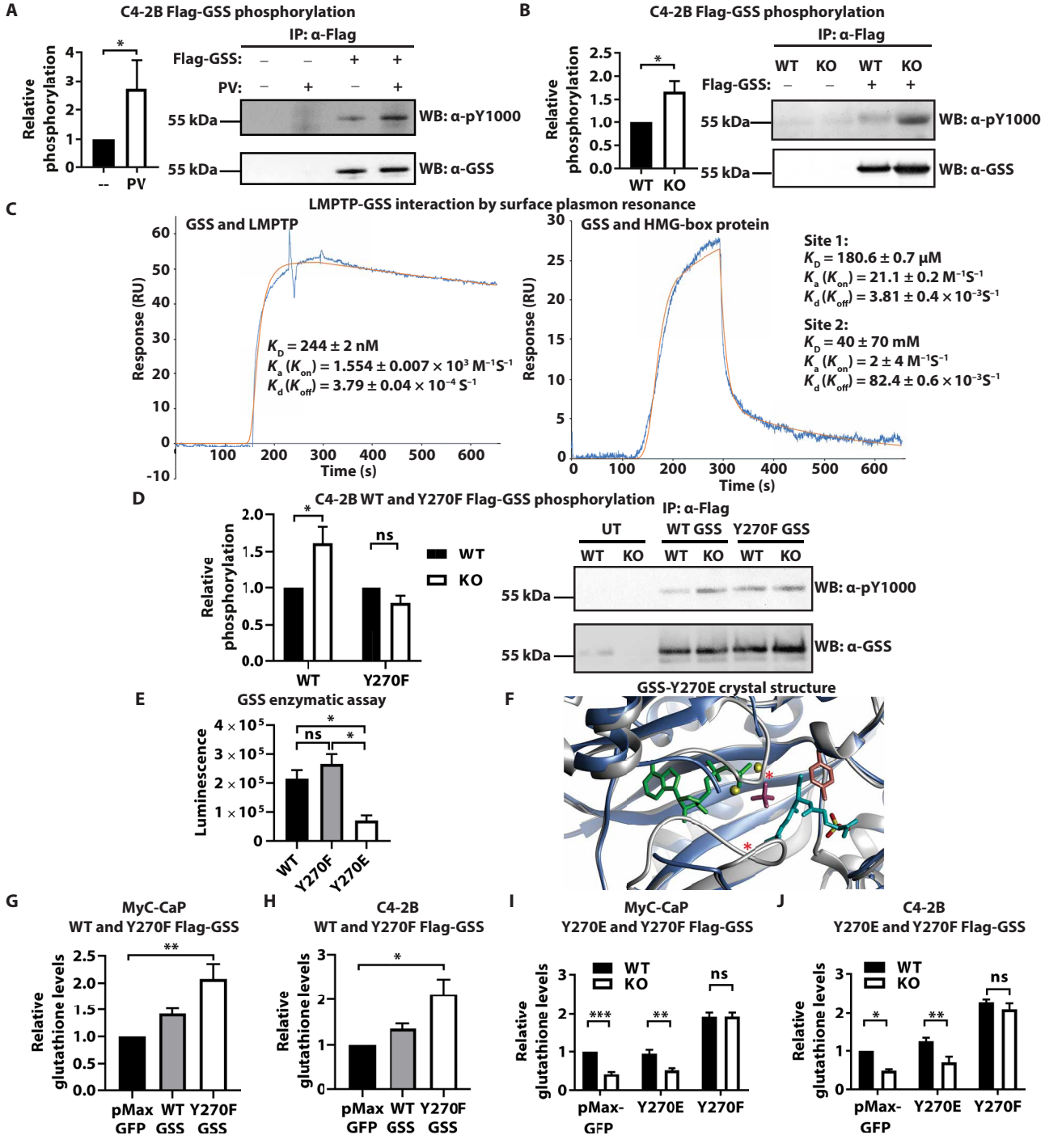

Fig. 5. LMPTP blocks GSS activity via dephosphorylation on Tyr^{270}. (**A**, **B**, and **D**) Western blot of α-Flag immunoprecipitations. Mean ± SEM pY1000/GSS relative signaling intensity from four independent experiments plus representative blots is shown. (A) C4-2B transfected with Flag-GSS and stimulated with 200 μM pervanadate (PV) or left unstimulated. (B) WT or LMPTP KO C4-2B transfected with Flag-GSS. (**C**) SPR sensograms. Kinetics data for GSS binding to LMPTP (left) and unrelated DNA-binding HMG-box protein (right). Blue and orange curves show analyte response curve and model fit, respectively. (D) WT or LMPTP KO C4-2B transfected with WT or Y270F Flag-GSS. (**E**) In vitro GSS enzymatic activity assay (WT: $n = 6$; Y270E: $n = 3$; Y270F: $n = 3$). (**F**) Glutathione binding site in the structure of unliganded GSS in ribbon representation (blue) with superposed 2HGS (gray). ADP (green), sulfate (pink), glutathione (cyan), Mg^{2+} ions (yellow), and Tyr^{270} side chain (brown) from 2HGS are shown as well as sulfate ions in the current structure (yellow/red). Red asterisks denote two loops partially disordered in the unliganded structure. Molecular graphics were performed with UCSF Chimera (*67*). (**G** to **J**) Glutathione levels detected from four independent experiments as in Fig. 4 (H to K). (G) and (H) MyC-CaP (G) or C4-2B (H) transfected with WT or Y270F Flag-GSS. Mean ± SEM relative concentrations of glutathione. (I) and (J) WT or LMPTP KO MyC-CaP (I) or C4-2B (J) transfected with Y270E or Y270F Flag-GSS. Mean ± SEM concentrations of glutathione. ns, nonsignificant. *$P < 0.05$, **$P < 0.01$, and ***$P < 0.001$, Mann-Whitney *U* test [(A) and (B)], unpaired *t* test with Welch's correction (D), one-way ANOVA with Tukey's method [(E), (G), and (H)], and one-way ANOVA with Šidák method [(I) and (J)]. IP, immunoprecipitation.

retained their phenotype of deficient glutathione production compared to WT cells, while overexpression of phosphorylation-deficient GSS-Tyr^{270}Phe abolished the difference in glutathione production between WT and LMPTP KO cells (Fig. 5, I to J). Together, these results suggest that LMPTP promotes glutathione production in PCa cells by dephosphorylating GSS on Tyr^{270} and enhancing GSS enzymatic activity and glutathione production.

Exogenous GSH overcomes defective growth and invasiveness of LMPTP KO PCa cells

We next sought to determine whether defective glutathione production mediates the reduced growth and invasiveness of LMPTP KO PCa cells. To do so, we assessed whether rescuing the deficient glutathione levels in LMPTP KO cells with exogenous glutathione could overcome the effects of LMPTP deletion on PCa cell growth and invasion. For these experiments, we used glutathione monoethyl ester (GSH-MEE), a cell-permeable glutathione derivative that is hydrolyzed intracellularly by esterases, yielding glutathione (*37*). Treatment of MyC-CaP and C4-2B cells with GSH-MEE abolished the differences in growth (Fig. 6, A and B) and invasion (Fig. 6, C and D) between WT and LMPTP KO cells. Together, these data support the idea that LMPTP promotes PCa cell growth and metastasis through its action as a key promoter of glutathione synthesis.

Loss of LMPTP promotes PCa cell eIF2 signaling and DNA damage

We next explored how defective glutathione production could affect signaling pathways controlling the functions of PCa cells. We performed phosphoproteomics of WT and LMPTP KO MyC-CaP and C4-2B cells using three KO MyC-CaP cell lines and four KO C4-2B cell lines. Each cell line was plated in triplicate and allowed to adhere overnight before lysis (scheme shown in Fig. 7A). Canonical pathway analysis of phosphoproteins displaying $\log_2$(LMPTP KO/WT signal ratio) < -0.59 or > 0.59 using the Core Analysis function in the QIAGEN Ingenuity Pathway Analysis (IPA) platform revealed Molecular mechanisms of cancer and EIF2 signaling as the top 2 significantly altered pathways in LMPTP KO cells (Fig. 7B). Because the EIF2 signaling pathway is a component of the molecular mechanisms of cancer pathway, we focused our attention on this pathway. Eukaryotic initiation factor 2 (eIF2) is a regulator of the cellular integrated stress response (ISR) (*38*). This pathway is triggered in response to cellular stressors such as oxidative stress and is activated by phosphorylation of eIF2 on Ser^{51}. We assessed eIF2-Ser^{51} phosphorylation in LMPTP KO MyC-CaP and C4-2B cells in response to a short (2 hours) serum starvation. We observed increased eIF2-Ser^{51} phosphorylation in LMPTP KO versus WT cells (Fig. 7C and fig. S9), suggesting that the eIF2 ISR pathway is activated in LMPTP KO cells. To confirm this, we assessed expression of the transcription factors activating transcription factor 4 (ATF4) and nuclear factor erythroid 2–related factor 2 (NRF2), which are induced following eIF2-Ser^{51} phosphorylation (*39*), as downstream readouts of ISR activation. LMPTP KO MyC-CaP cells showed significantly enhanced expression of both transcription factors at the mRNA (Fig. 7, D and E) and protein (Fig. 7, F to H) levels compared to WT cells following serum starvation. LMPTP KO C4-2B cells also showed significantly enhanced *ATF4* and *NRF2* mRNA levels, as well as NRF2 protein, and a trend toward increased ATF4 protein levels (fig. S9). Furthermore, we analyzed phosphorylation levels of eIF2-Ser^{51} in MyC-CaP tumors from mice treated with LMPTP inhibitor Compd. 23 (shown in Fig. 2E) and found significantly increased eIF2-Ser^{51} phosphorylation in tumors from mice treated with LMPTP inhibitor chow compared to mice fed regular chow (Fig. 7I).

Because excessive oxidative stress can lead to increases in DNA damage (*40*), we also assessed whether LMPTP KO PCa cells display increased levels of DNA damage using phosphorylation of H2A histone family member X (H2AX) on Ser^{139} as a readout (*40*). As shown in Fig. 7J, LMPTP KO MyC-CaP cells show significantly more H2AX-Ser^{139} phosphorylation than WT MyC-CaP. Although we did not observe enhanced apoptosis/necrosis in LMPTP KO cells following annexin V/propidium iodide staining (fig. S10), cell cycle phase analysis by propidium iodide staining of fixed cells revealed enhanced percentages of LMPTP KO cells in the G_2-M phase compared to WT cells (Fig. 7K). These results suggest that increased percentages of LMPTP KO cells undergo G_2-M phase arrest and are consistent with an inability of these cells to repair damaged DNA (*40*). Together, these data suggest that loss of LMPTP leads to increased activation of the eIF2-mediated stress response and enhanced DNA damage in PCa cells, two phenotypes that are consistent with reduced protection against reactive oxygen species (ROS) damage caused by deficiency of glutathione.

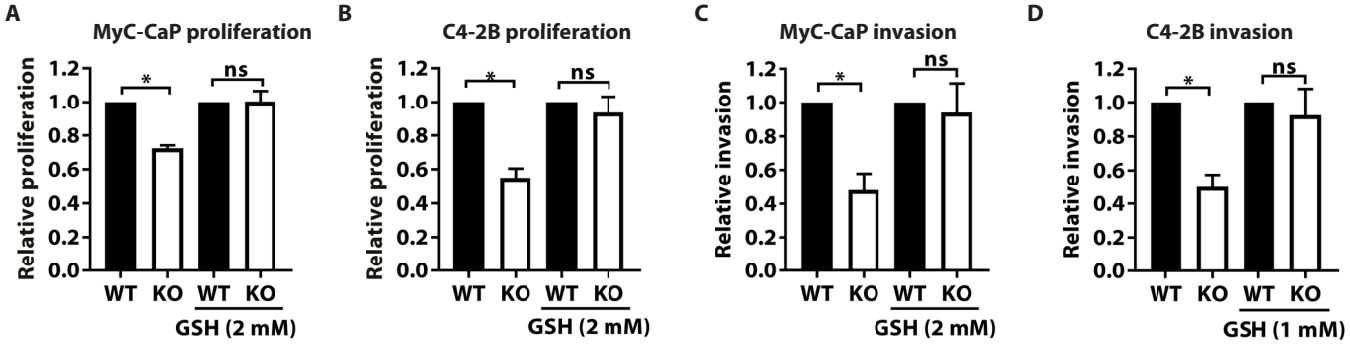

Fig. 6. Exogenous GSH abolishes the differences in growth and invasion between WT and LMPTP KO PCa cells. (**A** and **B**) Growth assays of WT and LMPTP KO MyC-CaP (A) and C4-2B (B) cells performed as in Fig. 2 (A and B) in the presence or absence of GSH-MEE or vehicle. (**C** and **D**) Invasion assays of WT and LMPTP KO MyC-CaP (C) and C4-2B (D) cells performed as in Fig. 3 (A and B) in the presence of GSH-MEE or vehicle. (A) to (D) Mean ± SEM proliferation [(A) and (B)] or invasion [(C) and (D)] relative to the WT cells for each condition from four independent experiments is shown. ns, nonsignificant. *$P < 0.05$, Mann-Whitney *U* test.

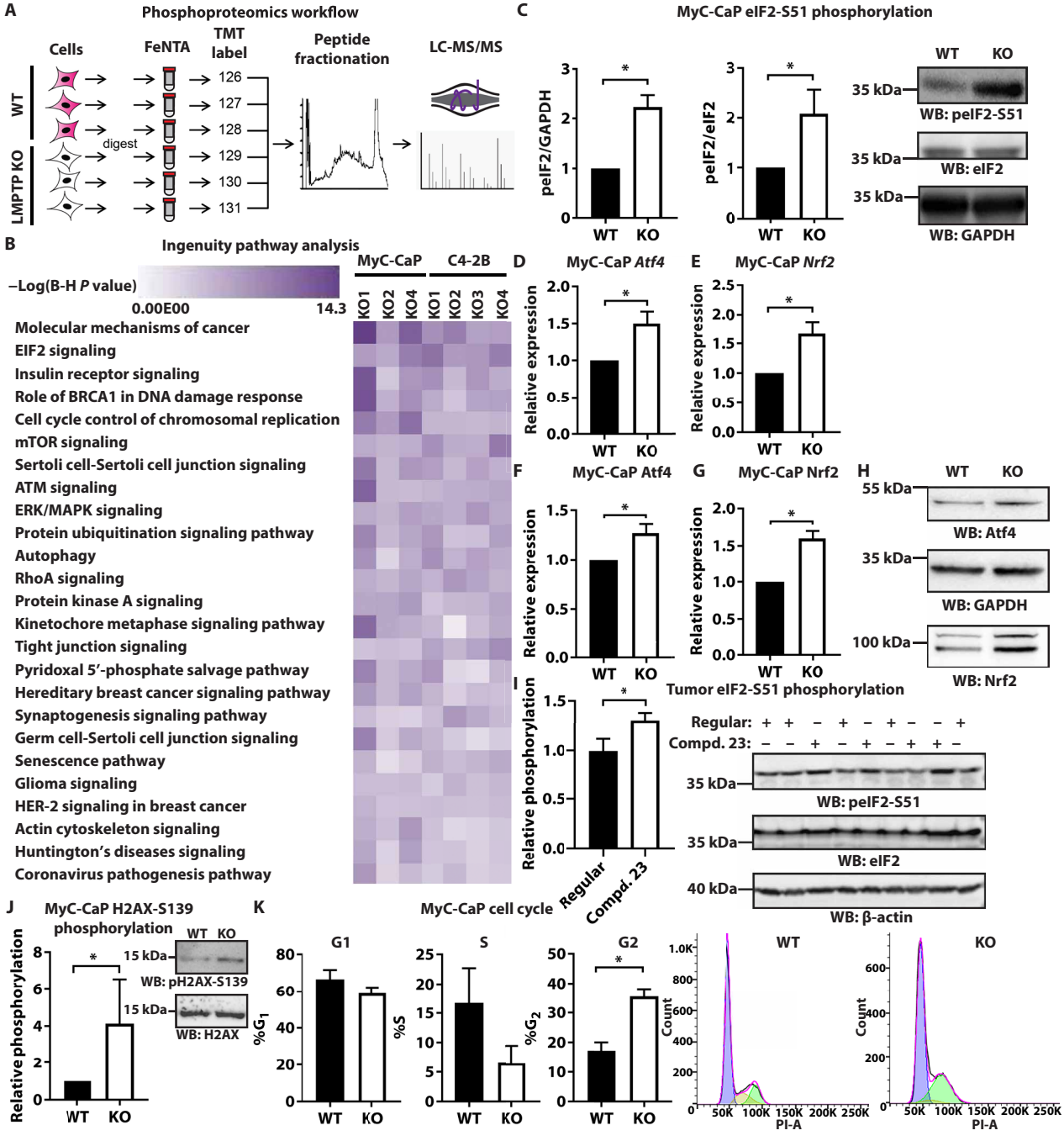

Fig. 7. Loss of LMPTP promotes PCa cell eIF2 signaling. (**A** and **B**) WT and LMPTP KO MyC-CaP and C4-2B cells were grown overnight and lysed in 9 M urea, reduced, alkylated, and digested, and samples were passed through an FeNTA column. Samples were tandem mass tag (TMT) labeled–pooled and analyzed by LC-MS/MS. (A) Scheme of phosphoproteomics workflow. (B) Pathway analysis using Core Analysis in Ingenuity Pathway Analysis (IPA) platform of phosphoproteins displaying $\log_2$(KO/WT) signal ratio > |0.59| and $P < 0.05$. Pathways were ranked according to $-\log_{10}(P$ value). Top 25 canonical pathways are shown. (**C**) Eukaryotic initiation factor 2 (eIF2)-Ser[51] phosphorylation assessed in WT and LMPTP KO MyC-CaP cells via WB after 2-hour serum starvation. Left: Mean ± SEM ratio of peIF2/eIF2 and peIF2/GAPDH signaling intensity relative to the WT sample. (Right) Representative blots. (**D** to **H**) Atf4 [(D) and (F)] and Nrf2 [(E) and (G)] expression levels assessed in MyC-CaP cells after 4-hour serum starvation. (D) and (E) Mean ± SEM mRNA expression assessed by qPCR and normalized to *POLR2A*. (F) and (G) Mean ± SEM protein expression assessed by WB and normalized to GAPDH. (H) Representative blots. (**I**) eIF2-Ser[51] phosphorylation assessed in tumors of mice treated with Compd. 23 or regular chow (mice from Fig. 2E; one tumor was removed as an outlier following the Grubbs test). Left: Mean ± SEM ratio of peIF2/eIF2 signaling intensity. Right: peIF2-Ser[51], eIF2, and β-actin blots. (**J**) H2A histone family member X (H2AX)–Ser[139] phosphorylation assessed in WT and LMPTP KO MyC-CaP cells via WB following overnight serum starvation. Left: Mean ± SEM ratio of pH2AX-Ser[139]/H2AX signaling intensity. Right: Representative blots. (**K**) Cell cycle phases of WT and LMPTP KO MyC-CaP cells were determined by flow cytometry following propidium iodide staining. Left: % cells in G_0-G_1, S, or G_2-M phase. Right: Representative histograms fit with Dean-Jett-Fox model. *$P < 0.05$, Mann-Whitney *U* test [(C) to (G) and (J) and (K)], and unpaired *t* test (I). (C) to (G) and (J) and (K) Data are from four independent experiments.

Loss of LMPTP enhances taxane-induced ROS production and sensitizes PCa to taxanes

Because LMPTP deletion leads to deficient glutathione production and induction of ROS-dependent damage, we reasoned that loss of LMPTP activity might also sensitize PCa cells to anticancer drugs that induce ROS generation by impairing the cell's ability to respond to drug-induced ROS-dependent insults. The commonly used taxane drugs, docetaxel and cabazitaxel, are reported to enhance intracellular production of ROS (*41*, *42*). Inhibition of DNA damage repair also reportedly promotes sensitivity of PCa to these two drugs (*43*). We assessed the effect of LMPTP KO on ROS levels in MyC-CaP treated with either docetaxel or cabazitaxel. Both taxanes significantly enhanced ROS levels in MyC-CaP cells, and LMPTP deletion substantially enhanced the levels of ROS in cells treated with either taxane (Fig. 8A). We next asked whether deletion of LMPTP would sensitize PCa cells to growth inhibition by docetaxel and cabazitaxel. As shown in Fig. 8, B to E, LMPTP deletion combined with taxane treatment significantly reduced the growth of MyC-CaP and C4-2B cells, possibly by impairing the ability of the cells to mitigate the damaging effects of excessive oxidative stress.

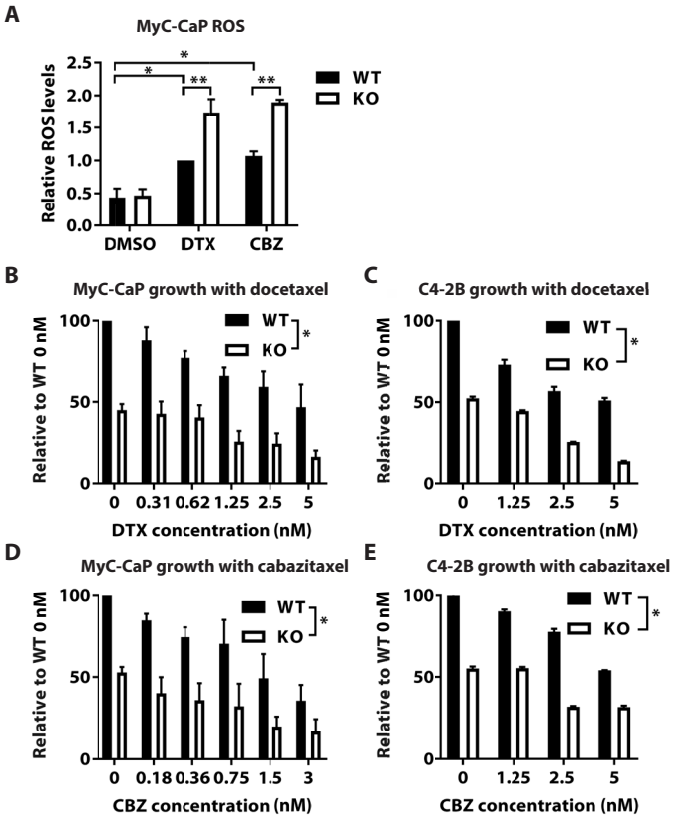

Fig. 8. Loss of LMPTP activity sensitizes PCa cells to taxane drugs. (**A**) WT or LMPTP KO MyC-CaP cells were treated with 2.5 nM docetaxel (DTX) or 1.5 nM cabazitaxel (CBZ) or DMSO for 4 hours. ROS detection was performed using a fluorescent ROS detection assay. (**B** to **E**) WT or LMPTP KO MyC-CaP [(B) and (D)] or C4-2B [(C) and (E)] cells were plated and allowed to grow. After 3 days, cells were treated with varying concentrations of docetaxel [(B) and (C)] or cabazitaxel [(D) and (E)]. Growth was quantified on day 5 as described in Fig. 2 (A and B). $*P < 0.05$ and $**P < 0.01$, two-way ANOVA.

DISCUSSION

We report a mechanistic investigation into the role of LMPTP in PCa. *ACP1* up-regulation has been reported for prostate tumors, although a potential pathogenic role has not been addressed. Here, we further examined *ACP1* expression in prostate tumors and sought to understand its role in prostate tumor cell biology. Examination of *ACP1* expression in prostate tumor tissue from the TCGA database and our analysis of samples from the PCBN confirmed previous reports of *ACP1* up-regulation in prostate tumor tissue. Within tumor samples, *ACP1* expression is further up-regulated in tumors reflective of increased cancer severity, including higher Gleason scores, the presence of metastasis, and luminal versus basal subtype, suggesting that *ACP1* expression positively associates with severity of disease in PCa. Concordantly, analysis of two large, independent datasets substantiated that higher *ACP1* expression in prostate tumors correlates with reduced overall patient survival. Together, these findings suggest *ACP1* as a potential biomarker for clinical prognosis in PCa.

To understand whether LMPTP plays an active pathogenic role in PCa, we used CRISPR-Cas9 to generate LMPTP KO MyC-CaP and C4-2B prostate tumor cell lines. Using this approach, we found that loss of LMPTP reduces PCa cell growth in vitro and in vivo, supporting the notion that LMPTP expression is necessary for aggressive prostate tumor growth. To understand whether the tumor-promoting action of LMPTP is dependent on its catalytic activity, we used an orally bioavailable pharmacological inhibitor. Inhibition of LMPTP's catalytic activity substantially impaired the growth of prostate tumors in vivo, indicating potential for LMPTP as a therapeutic target for PCa.

We also explored the role of LMPTP in metastatic features of PCa, including invasiveness, anchorage-independent growth, and ability to grow in the bone. Loss of LMPTP reduced all of these features in vitro. Both LMPTP deletion and pharmacological inhibition impaired the ability of prostate tumors to grow in bone in vivo. Although we cannot rule out that loss of LMPTP inhibits PCa metastatic phenotypes, at least in part, as a consequence of inhibited cell proliferation, together, these data suggest that inhibiting LMPTP could be a potential strategy for treating both localized and metastatic prostate tumors.

To uncover the mechanism by which LMPTP supports the growth of PCa cells, we performed metabolomics in LMPTP KO MyC-CaP and C4-2B cells to identify perturbations in cells lacking LMPTP. Using independent cell types allowed us to select pathways likely to be specifically altered by LMPTP deletion, thus reducing potential off-target or clonal effects. Because LMPTP KO cells displayed GSH but excessive levels of glutathione precursor γ-glutamylcysteine in MyC-CaP or 5-oxoproline in C4-2B, we focused on GSS—the enzyme responsible for catalyzing the production of glutathione from γ-glutamylcysteine and glycine. A search of the PhosphoSite database revealed evidence of GSS phosphorylation on Tyr^{270}, although the function of this phosphorylation was not yet reported. We found GSS to be tyrosine phosphorylated in PCa cells and to be enhanced by LMPTP KO. Furthermore, we found that mutating Tyr^{270} abolished the difference in phosphorylation between WT and LMPTP KO cells. In vitro, phospho-mimetic Tyr^{270}Glu mutation of recombinant GSS abolished its ability to catalyze glutathione synthesis. Overexpression of Tyr^{270}Phe-mutated GSS strongly enhanced glutathione levels in PCa cells and, importantly, overcame the defect in glutathione production in LMPTP KO cells.

Conversely, overexpression of phospho-mimetic Glu^{270}-mutated GSS had no effect on glutathione levels in WT or LMPTP KO cells. Ultimately, we found that treatment with exogenous GSH-MEE rescued the defects in growth and invasiveness of LMPTP KO cells, supporting the importance of LMPTP's role in glutathione production in promoting PCa cell growth and metastasis. Although deeper metabolic studies using isotype-labeling are needed to formally conclude that LMPTP promotes glutathione synthesis rather than altering its levels through consumption or degradation, together, our data strongly suggest that LMPTP is a key promoter of GSS function and glutathione levels in PCa cells.

The role of LMPTP in PCa cell glutathione production was further supported by phosphoproteomics analysis, which revealed strong changes in the eIF2-driven ISR. Confirmatory experiments demonstrated up-regulation of the eIF2 pathway, suggesting that LMPTP KO cells were undergoing excessive oxidative stress in response to deficient glutathione levels. This was reflected in the enhanced eIF2-Ser^{51} phosphorylation and ATF4 and NRF2 levels in LMPTP KO PCa cells and in enhanced eIF2-Ser^{51} phosphorylation in prostate tumors from mice treated with LMPTP inhibitor. This concept is also supported by the sensitizing effects of LMPTP deletion/inhibition in PCa cells on the growth inhibitory effects of taxane drugs, which enhance ROS production (*41*, *42*). Phosphoproteomics also revealed the cell cycle control of chromosomal replication pathway was significantly altered in all LMPTP KO clones tested, consistent with our findings that enhanced percentages of LMPTP KO cells undergo cell cycle arrest in the G_2-M phase. Further experiments are needed to confirm whether LMPTP attenuates the ISR in PCa cells entirely through its action on glutathione production or through additional mechanisms as well.

We propose a model (Fig. 9) by which LMPTP supports PCa cell glutathione production by dephosphorylating GSS on inhibitory phosphorylation site Tyr^{270}. Dephosphorylation of this site by LMPTP enhances GSS catalytic activity and glutathione production, enabling PCa cell survival, growth, and invasiveness by reducing cellular oxidative stress. We also do not exclude the possibility of additional GSS phosphorylation sites or pathways under control of LMPTP promoting the growth and metastasis of PCa cells.

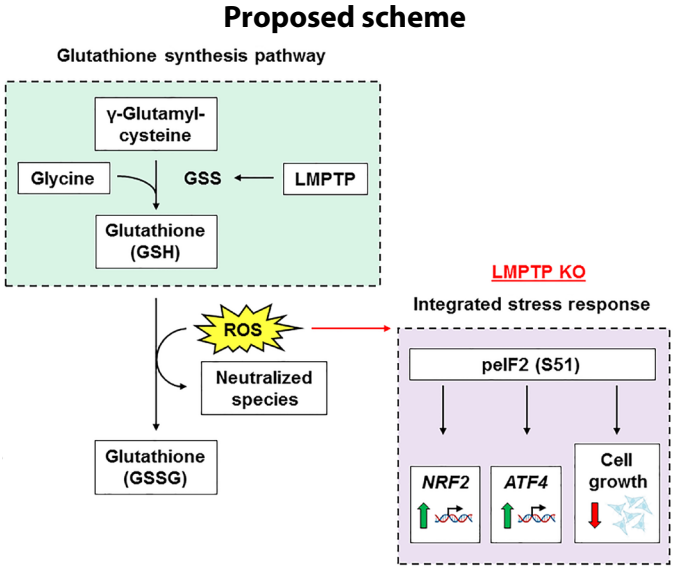

Fig. 9. Scheme of proposed mechanism. Proposed model by which LMPTP supports PCa cell glutathione production by dephosphorylating GSS on inhibitory phosphorylation site Tyr^{270}. Dephosphorylation of this site by LMPTP enhances GSS catalytic activity and glutathione production, enabling PCa cell survival, growth, and invasiveness by reducing cellular oxidative stress.

Tyr^{270} is localized in the substrate binding "S loop" of GSS, an 11 residue stretch (Phe^{266}-Arg^{267}-Asp^{268}-Gly^{269}-Tyr^{270}-Met^{271}-Pro^{272}-Arg^{273}-Gln^{274}-Tyr^{275}-Ser^{276}) participating in γ-glutamylcysteine binding (*44*). GSS Tyr^{270}Cys and Tyr^{270}His mutations were found by sequencing patients with GSS deficiency, a disorder characterized by deficiency in glutathione levels, metabolic acidosis, 5-oxoprolinuria, and increased hemolytic rate (*45*). Both patients with mutated Tyr^{270} showed substantially reduced GSS enzymatic activity (*45*). Mutations in the S loop Arg^{267} have also been reported in patients with GSS deficiency (*46*). These data suggest that alterations in this region such as phosphorylation or mutation can inhibit the ability of GSS to bind its substrate, leading to defective glutathione production. Our crystal structure of GSS Tyr^{270}Glu indicates that this residue would not be easily accommodated into the active site of kinases or phosphatases despite being somewhat more accessible due to the disordering of two active site loops. It could, however, become involved in signaling via posttranslational modifications if alternative conformations become energetically favorable under appropriate cellular conditions.

Our findings suggest that LMPTP promotes prostate tumor growth, at least in part, through up-regulation of glutathione production. Elevated cancer cell glutathione levels are associated with tumor progression and resistance to chemotherapeutic drugs (*47*). By increasing glutathione levels, cancer cells can potentially mitigate the impacts of oxidative stress resulting from high metabolic rates. Although we observe enhanced eIF2-Ser^{51} phosphorylation in tumors of mice treated with LMPTP inhibitor, further studies are needed to more definitively confirm that the inhibitor's effects on tumor growth in vivo are through direct inhibition of GSS activity and GSH production. Furthermore, it is possible that LMPTP plays a similar function in other types of tumors displaying up-regulation of LMPTP expression, such as in the case of CRC (*20*–*22*), and further experimentation is necessary to understand whether LMPTP regulates oxidative stress in other nontumor and tumor cell types. It is also possible that LMPTP promotes tumor growth through additional mechanisms unrelated to oxidative stress and via dephosphorylation of additional substrates.

Another open question is which pathway underlies *ACP1* up-regulation in prostate tumor cells and whether oxidative stress is somehow involved in LMPTP transcriptional regulation. The potential oxidative inactivation of LMPTP—which is believed to be regulated by glutathione (*48*)—could also play into the observed relationship between the LMPTP expression and glutathione levels in PCa cells. As with most other PTPs, LMPTP can be inactivated by oxidation of its catalytic Cys^{13}. LMPTP belongs to a restricted subgroup of PTPs whose redox inactivation is reversible because a disulfide bridge can be formed between Cys^{13} and Cys^{18} in the P loop of the enzyme (*49*). It is tempting to speculate about the existence of an oxidative stress rheostat that operates through a balance between LMPTP expression, which tends to protect cells from oxidative stress, and LMPTP inactivation by ROS, which would tend to reduce glutathione levels.

In conclusion, using a combination of cell-based, in vivo, metabolomic, and phosphoproteomic approaches, we report a role for LMPTP as a key promoter of PCa glutathione production, growth,

and metastasis. We find that LMPTP inhibition impairs primary and bone metastatic tumor growth. Further investigation of the functions of LMPTP in PCa cell biology is warranted to understand the potential of targeting LMPTP for treatment of primary and metastatic prostate tumors.

MATERIALS AND METHODS

Analysis of *ACP1* expression in TCGA

ACP1 expression in PRAD from TCGA was obtained from the UALCAN web portal (*50*) or the UCSC Xena browser (*51*).

Analysis of *ACP1* expression in the Caris Life Sciences cohort

Study cohort

Formalin-fixed paraffin-embedded (FFPE) samples from patients with PCa ($N = 5028$) were submitted by clinical physicians to a commercial Clinical Laboratory Improvement Amendments of 1988-certified laboratory for molecular profiling (Caris Life Sciences, Phoenix, AZ). The present study was conducted in accordance with the guidelines of the Declaration of Helsinki, Belmont Report, and U.S. Common Rule. With compliance to policy 45 CFR 46.101(b), this study was conducted using retrospective, deidentified clinical data, and patient consent was not required.

Clinical outcomes

Real-world overall survival information was obtained from insurance claims data and calculated from first the time of biopsy to last contact. Survival curves were compared using the log-rank test, and hazard ratios (HRs) with 95% confidence interval (CI) were estimated by Cox proportional hazards model.

RNA WTS

Whole transcriptome sequencing (WTS) uses a hybrid-capture method to pull down the full transcriptome from FFPE tumor samples using the Agilent SureSelect Human All Exon V7 bait panel (Agilent Technologies) and the Illumina NovaSeq platform (Illumina Inc.). FFPE specimens underwent pathology review to discern the percent tumor content and tumor size; a minimum of 10% tumor content in the area for microdissection was required to enable enrichment and extraction of tumor-specific RNA. A QIAGEN RNA FFPE tissue extraction kit was used for extraction, and the RNA quality and quantity were determined using the Agilent TapeStation. Biotinylated RNA baits were hybridized to the synthesized and purified cDNA targets, and the bait-target complexes were amplified in a post-capture PCR reaction. The resultant libraries were quantified and normalized, and the pooled libraries were denatured, diluted, and sequenced. Raw data were demultiplexed using the Illumina DRAGEN FFPE accelerator. FASTQ files were aligned with STAR aligner (Alex Dobin, release 2.7.4a github). A full 22,948 gene dataset of expression data was produced by the Salmon, which provides fast and bias-aware quantification of transcript expression. BAM files from STAR aligner were further processed for RNA variants using a proprietary custom detection pipeline. The reference genome used was GRCh37/hg19, and analytical validation of this test demonstrated ≥97% positive percent agreement, ≥99% negative percent agreement, and ≥99% overall percent agreement with a validated comparator method.

Antibodies and other reagents

LMPTP inhibitor Compd. 23 was generated as described (*14*) and formulated in rodent chow at 0.1% (w/w) by Research Diets. CRISPR-Cas9 plasmids were purchased from ATUM. Pierce D-Luciferin monopotassium salt was purchased from Thermo Fisher Scientific and reconstituted using phosphate-buffered saline (PBS). For in vitro experiments, docetaxel and cabazitaxel were purchased from Selleckchem and reconstituted in sterile dimethyl sulfoxide (DMSO). The anti–phospho–eIF2-Ser^{51} (#3398), anti-eIF2 (#9722), anti-NRF2 (#12721), anti-ATF4 (#11815), anti–glyceraldehyde 3-phosphate dehydrogenase (#5174), anti–phospho-H2AX (#9718), anti-H2AX (#2595), and anti-pTyr (pY1000; #8954) antibodies were purchased from Cell Signaling Technology (CST). The rabbit anti-LMPTP antibody was described in (*52*). The mouse anti-LMPTP antibody (#sc-100343) was purchased from Santa Cruz Biotechnology. The anti-GSS antibodies were purchased from Thermo Fisher Scientific (#PA5-89891) or Santa Cruz Biotechnology (#sc-166882). Anti-rabbit (#NA934-1ML) and anti-mouse (#NA931-1ML) secondary antibodies were purchased from Thermo Fisher Scientific. TrueBlot anti-rabbit (#RL18-8816-31) and anti-mouse (#RL18-8817-31) secondary antibodies were purchased from Rockland. GSH-MEE (#353905) was purchased from Sigma-Aldrich. Unless otherwise specified, chemicals and other reagents were purchased from Sigma-Aldrich.

Cell culture and stimulation

Mouse MyC-CaP (*53*) and luciferase-expressing MyC-CaP (MyC-CaP/GFP-Luc) (*54*) PCa cells were grown in Dulbecco's minimal essential medium (DMEM) supplemented with 10% fetal bovine serum (FBS) and penicillin (100 U/ml) and streptomycin (100 μg/ml; 1X Pen/Strep). Both cell lines were confirmed to be negative for mycoplasma, lymphocytic choriomeningitis virus, lactate dehydrogenase virus, mouse hepatitis virus, and mouse parvovirus by IDEXX Bioanalytics. Human C4-2B PCa cells were purchased from American Type Culture Collection and were grown on 0.01% polylysine–coated tissue culture plates in RPMI 1640 supplemented with 10% FBS and 1X Pen/Strep. All cells were maintained in a sterile incubator at 37°C and 5% CO_2. For serum starvation, cells were cultured in growth media with 0.1% FBS. For pervanadate stimulation, cells were treated with 200 μM pervanadate for 15 min at 37°C before lysis.

LMPTP KO cell generation

Guide RNA (gRNA) targeting exon 1 of either human or mouse *ACP1* locus was selected using ATUM's CRISPR gRNA Design Tool. Plasmids encoding the gRNA, Cas9 endonuclease, kanamycin resistance sequence, and fluorescent protein [green fluorescent protein (GFP) for MyC-CaP and C4-2B and red fluorescent protein (RFP) for MyC-CaP/GFP-Luc] for mammalian selection were purchased from ATUM. MyC-CaP and C4-2B cells were grown in six-well plates and transfected at ~50 to 60% confluency with 500 ng of plasmid DNA using Lipofectamine 3000 (Life Technologies) following the manufacturer's instructions. Two days after transfection, cells were collected and resuspended in ice-cold fluorescence-activated cell sorting buffer (25 mM Hepes, 1 mM EDTA, and 1% FBS in PBS). GFP$^+$ MyC-CaP or C4-2B cells and RFP$^+$ MyC-CaP/GFP-Luc cells were single-cell–sorted into 96-well plates containing growth media and allowed to grow for characterization.

GSS overexpression

Plasmid expressing human Myc-DDK (Flag)–tagged GSS under the cytomegalovirus promoter was purchased from OriGene

(#RC203174) and used as the template for site-directed mutagenesis to generate GSS point mutants at Tyr^{270}. MyC-CaP and C4-2B WT or LMPTP KO cells were transfected with WT GSS, Tyr^{270}Phe GSS, or Tyr^{270}Glu GSS plasmids or pMax-GFP plasmid (Lonza) at ~70 to 80% confluency using Lipofectamine 3000 (Life Technologies) or FUGENE4K transfection reagents (Fugent LLC) following the manufacturer's instructions. Cells were lysed for immunoprecipitation or glutathione detection assay after 24 hours.

Cell lysis, immunoprecipitation, and Western blotting

Cells were lysed in 1X cell lysis buffer (CST) with 1 mM phenylmethylsulfonyl fluoride (PMSF). For Western blotting and immunoprecipitation of lysates, protein concentrations were determined using the Pierce BCA Protein Assay Kit (Thermo Fisher Scientific). For analysis of ATF4 and NRF2 protein levels in MyC-CaP, cells were lysed in buffer containing 50 mM tris-HCl (pH 7.4), 150 mM NaCl, 0.5% sodium deoxycholate, 0.1% SDS, 1% Triton X-100, 1 mM EDTA, 1X protease inhibitor cocktail (Thermo Fisher Scientific), and 1 mM PMSF. Flag-tagged GSS was immunoprecipitated by rocking lysates with anti-Flag M2 Magnetic Bead Conjugate (Sigma-Aldrich, #M8823) for 2 hours, or unconjugated anti-Flag M2 antibody for 2 hours followed by addition of protein G sepharose beads for an additional hour. Immunoprecipitates were washed in 1X lysis buffer with PMSF and subjected to Western blotting. For pTyr immunoprecipitations, lysates were first denatured using 1% SDS at room temperature for 15 min then diluted with lysis buffer to a final concentration of 0.1% SDS. Phosphorylated proteins were immunoprecipitated by rocking lysates with anti-pY1000 Sepharose Bead Conjugate (CST, #14500S) for 2 hours, or unconjugated anti-pY1000 antibody for 2 hours followed by addition of protein G sepharose beads for an additional hour. Immunoprecipitates were washed and subjected to Western blotting. For Western blotting, samples were resuspended in 2X or 6X Laemmli sodium dodecyl sulfate (SDS) sample buffer (BioRad or Thermo Fisher Scientific) with the addition of 5% β-mercaptoethanol. In some experiments on GSS in protein lysates or immunoprecipitates, 50 mM dithiothreitol was added to the SDS sample buffer along with 5% β-mercaptoethanol. Precast Tris-glycine gels were purchased from Thermo Fisher Scientific. Western blot signals were quantified using ImageJ software.

Cell proliferation assay

WT and LMPTP KO MyC-CaP or C4-2B cells were plated in triplicate at equal counts into 12 well plates. Cells were left to grow for 5 days undisturbed except for replenishing the media after three days. After 5 days of growth, cells were fixed with 70% ethanol and stained with 0.05% crystal violet in 25% ethanol. Plates were gently rinsed with deionized water and left to dry overnight away from light. Crystal violet was extracted using Sorenson's extraction reagent (50 mM sodium citrate & 50 mM citric acid dissolved in 50% ethanol). Extracted solution was diluted anywhere between 1:2 and 1:10. Absorbance of the samples was read in triplicate at 595 nm using the Tecan Infinite F Plex plate reader. For experiments with docetaxel or cabazitaxel, cells were treated with 0.3125–5 nM docetaxel or 0.1825–3 nM cabazitaxel or DMSO on day 3.

Mice

Animal experiments were conducted in accordance with Institutional Animal Care and Use Committee approved protocols at the University of California, San Diego (S16098) and the La Jolla Institute for Allergy & Immunology (AP00001013). CB-17 SCID mice were purchased from Taconic (#CB17SC). Since PCa only occurs in males, only male mice were used for experimentation.

Tumor xenograft mouse model

7–8 week old CB-17 SCID mice were assigned randomly into groups and injected subcutaneously in the right and left dorsal flanks with 200 K WT or LMPTP KO MyC-CaP cells suspended in 50% Matrigel Matrix Phenol Red Free (BD, #3562377) and 50% DMEM at a final volume of 100 μl. Tumor length, width, and depth were measured 3 times per week using a caliper starting 7 days after initial inoculation to calculate tumor volume, and the volume of the 2 tumors was averaged for each mouse. Mice were also weighed for the duration of the study. Study endpoint was defined as when a tumor reached 1.5–2 cm in diameter or a mouse lost 20% of its initial body weight. For the LMPTP inhibition study, mice were injected with 200 K WT MyC-CaP cells and 2 weeks later placed on chow formulated with 0.1% w/w Compd. 23 or regular chow. Following termination of the study, tumors were extracted and flash-frozen. For analysis of tumor eIF2-Ser^{51} phosphorylation levels, tumors were lysed in buffer containing 50 mM Tris-HCl pH 7.4, 150 mM NaCl, 0.5% sodium deoxycholate, 0.1% SDS, 1% Triton X-100, 1 mM EDTA, 1 mM sodium fluoride, 1 mM sodium orthovanadate, 1X protease inhibitor cocktail, and 1 mM PMSF, and lysates subjected to Western blotting.

Soft agar colony formation assay

A 1:1 ratio of 1.2% w/w noble agar (VWR, #90000–772) to 2X DMEM or RPMI media was plated on the bottom of 6 well plates. After solidification of the agar, MyC-CaP or C4-2B PCa cells were suspended in a 1:1 mixture of 0.6% noble agar to 2X DMEM or RPMI media and plated on top (35 K MyC-CaP cells/well and 20 K C4-2B cells/well). After solidification of the top layer, growth media with 10% FBS was added to each well to prevent gel agar from drying. Plates were maintained at 37°C and 5% CO_2 while maintaining a thin layer of growth media. After 21 days, colonies were stained with crystal violet and washed. Colonies were visualized and counted throughout the depth of the agar using the Motic AE2000 Inverted Microscope. Representative images were captured using the AxioVert Marianas Microscopy System as Z-stacks and compiled into a single image using ImageJ (*55*).

Matrigel invasion assay

WT and LMPTP KO MyC-CaP and C4-2B PCa cells were serum starved overnight (18 hours) in DMEM or RPMI media containing 0.1% FBS with 1X Pen/Strep. Cells were placed in the top chamber of a Matrigel Invasion Chamber (Corning, #354480) with the bottom chamber containing DMEM or RPMI media with 10% FBS with 1X Pen/Strep to promote migration. For experiments with LMPTP inhibitor, 10 μM Compd. 23 or DMSO was added to the top chamber. Two days later, cells on the bottom of the transwells were fixed with 100% methanol and stained using 0.05% crystal violet in 25% ethanol. Migrated cells were imaged using the Motic AE2000 Inverted Microscope and counted from 5 non-overlapping frames.

Bone mimetic environment growth assay

Generation of BME

BME were generated as previously reported (*29*). Briefly, scaffolds (area, 0.32 cm^2) were designed using computer-aided BioCAD

design software (RegenHU, Switzerland) according to the following characteristics: filament width of 35 μm, pore size of 40 μm and scaffold height of 320 μm. PCL (43 kDa, Polysciences) was melted at 85°C, and printed at a collector velocity of 40 mm s^{-1}, 5.0 kV, 1.0 bar, and at a collector distance of 10 mm using a 3DDiscovery Evolution printer (RegenHU). PCL scaffolds were stored in 70% ethanol until cell seeding. Human mesenchymal stem cells (hMSCs) were detached with trypsin, counted and seeded on the scaffold (2.5×10^5 cells in 25 μl of complete hMSC culture medium, 37°C, 5% CO_2, overnight); the day after, osteogenic medium was added to induce osteoblastic differentiation of hMSCs. BMEs were incubated in osteogenic medium for at least 30 days, with a weekly refreshment, to achieve osteoblastic differentiation and calcified matrix deposition.

Generation, seeding and analysis of C4-2B spheroids

Spheroids of C4-2B cells were generated using the hanging-drop method as previously described (*29*). Briefly, 25 μl drops containing 500 WT or LMPTP KO C4-2B cells were deposited on the lid of a 15 cm dish, inverted and incubated overnight at 5% CO_2, 37°C. The day after, spheroids were seeded on BMEs, as described above, in a 96 well plate. Cultures were incubated at 37°C, 5% CO_2 overnight and then overlaid with C4-2B culture medium. After 10 days, spheroid growth was monitored by imaging using a Leica MST66 confocal microscope. Quantification of spheroid size was performed by measuring the integrated density (area tumoroid x mean grey background) using ImageJ (*55*) as reported (*29*). For experiments with LMPTP inhibitor, 10 μM Compd. 23 or DMSO was added to the BME culture.

Intraosseous mouse model

8–10 week old CB-17 SCID male mice were anesthetized with isoflurane and 100 K WT or LMPTP KO MyC-CaP/GFP-Luc resuspended into 20 μl ice cold PBS were injected into the left tibia. Tumor growth was monitored over 10 weeks by injecting mice with 150 mg luciferin/kg body weight and imaging using the IVIS Spectrum in vivo imaging system. Images obtained from the IVIS were processed and quantified using Aura Imaging Software. For experiments using the LMPTP inhibitor, mice were administered regular chow or chow formulated with 0.1% w/w Compd. 23 starting 3 days before WT MyC-CaP/GFP-Luc cell injection.

Phosphoproteomics analysis

Sample preparation

WT and LMPTP KO MyC-CaP and C4-2B PCa cells were plated in triplicate in 15 cm plates overnight in growth media containing 10% FBS with 1X Pen/Strep. Cells were lysed in 9 M urea with Pierce protease/phosphatase inhibitor (#A32961), 10 μg/mL soybean trypsin inhibitor, 10 μg/ml aprotinin, 10 μg/ml leupeptin, 10 mM sodium orthovanadate, 5 mM sodium fluoride, 2 nM sodium pyrophosphate, and 1 mM PMSF and snap frozen.

Phosphopeptide enrichment and liquid chromatography with tandem mass spectrometry (LC-MS/MS)

Lysates were reduced, alkylated, digested to peptides and desalted before quantitative recovery of phosphopeptides using Fe-NTA columns (Thermo Fisher Scientific). Phosphopeptides from each condition were labeled with unique tandem mass tags and fractionated, followed by high performance LC-MS/MS. Post-acquisition data processing followed a well-validated pipeline of Comet/SEQUEST database searching, false discovery rate assessment and reporter ion quantification (*56, 57*). Phosphopeptide ratios were calculated as KO/WT and log-transformed. Canonical pathway analysis of phosphoproteins displaying log2(LMPTP KO/WT signal ratio) < −0.59 or > 0.59 and p-value <0.05 were performed using the Core Analysis function in the IPA platform (*58*).

Quantitative polymerase chain reaction

MyC-CaP and C4-2B cells were washed with PBS and lysed with RLT buffer (QIAGEN) containing 1:100 β-mercaptoethanol. RNA was extracted using RNeasy Kits (QIAGEN). cDNA was synthesized using the SuperScript III First-Strand Synthesis System (Thermo Fisher Scientific). Primer assays were purchased from QIAGEN or Sigma-Aldrich. qPCR was performed using a Bio-Rad CFX384 Touch Real-Time PCR Detection System. Reactions were measured in triplicate and data was normalized to the expression levels of the housekeeping gene RNA Polymerase II (*POLR2A*).

Metabolomics analysis

Sample preparation

WT and LMPTP KO PCa cells were grown in five replicates in 15 cm plates overnight the same way as prepared for phosphoproteomics analysis. For sample collection, the extracellular metabolome (media) along with intracellular metabolome (cell pellet) were retained and snap frozen.

UHPLC-MS

Intracellular metabolites were extracted using a modified Bligh-Dyer procedure as previously described (*16*, *59*). All metabolomics analyses were performed using a Q Exactive Hybrid Quadrupole Orbitrap Mass Spectrometer (Thermo Fisher Scientific) coupled to a Vanquish Horizon UHPLC system (Thermo Fisher Scientific). The MS was calibrated for mass accuracy before analysis and monitored throughout data acquisition to maintain mass accuracy below 5 ppm. A pooled quality control sample was injected between every batch of 6 samples to monitor instrument performance and guarantee consistency across the runs. Initial chromatographic separation of polar metabolites including nucleotides and redox cofactors was performed using an Atlantis Premier BEH Z-HILIC Column, 1.7 μm, 2.1 mm X 150 mm (Waters). The mobile phases used for this analysis were A) LCMS-grade water +10 mM ammonium acetate, B) 90:10 acetonitrile:LCMS-grade water +10 mM ammonium acetate (pH of 9.2), C) 100% acetonitrile. The following parameters were used for separation: sample injection volume: 5 μl; flow rate: 0.15 ml/min; flow gradient: 90:10 A:C for 7 min, 100% B for 10 min, 90:10 A:C for 18 min. After initial data acquisition, a CentriVap Benchtop Concentrator (Labconco) was used to dry the samples before they were resuspended in LCMS-grade water for secondary analysis of polyamines using a Kinetex C18 Column, 2.6 μm, 100 Å, 150 × 2.1 mm (Phenomenex). The mobile phases for this analysis were A) LCMS-grade water +0.2% formic acid, B) 100% methanol. The following parameters were used for separation: sample injection volume: 5 μl; flow rate: 0.15 mL/min; flow gradient: 98:2 A:B for 4 min, 20:80 A:B for 10 min, 2:98 A:B for 7 min, 98:2 A:B for 14 min. The nonpolar fractions were analyzed using the previously described method for targeted detection of CoQ9 and CoQ10 redox states (*60*). MS detection was performed in full scan mode with positive/negative switching and the following parameters: spray voltage: 3.0 kV; sheath gas: 45 units; auxiliary gas: 10 units; capillary temperature: 320°C, resolution: 70,000 at *m/z* ranges of 70–1000 and 50–750 for HILIC and Kinetex, respectively; max inject time: 200 ms, AGC target: 1E6, microscans: 1. The raw data files were

processed with SIEVE 2.2.0 software (Thermo Fisher Scientific) and the integrated peaks were mined against an in-house database of standards that includes the IROA Mass Spectrometry Metabolite Library of Standards (MSMLS; IROA Technologies) for accurate masses and retention times. The peaks were also matched to the accurate masses of the Human Metabolome Database (*61*).

Intracellular glutathione detection assay

WT and LMPTP KO MyC-CaP and C4-2B PCa cells were grown in normal cell culture conditions to 80% confluency then harvested using trypsin. For experiments with LMPTP inhibitor, 20 μM Compd. 23 or DMSO was added to the culture media for 48 hours before harvesting the cells. An intracellular glutathione detection assay was performed using the GSH/GSSG-Glo kit (Promega, #V6611) according to the manufacturer's instructions to assess total, oxidized, and GSH levels. Samples were analyzed in duplicate on opaque, white 96- well plates (Sigma-Aldrich). Bioluminescence was measured using the Tecan Infinite F Plex plate reader.

Purification of recombinant proteins

Human LMPTP-A was purified as previously reported (*14*). A codon-optimized open reading frame for bacterial expression of full-length WT GSS as a thrombin cleavable 6xHistidine N-terminal fusion in pET28a vector was purchased from Genscript. *Escherichia coli* BL21 (DE3) cell cultures were grown at 37°C in Luria-Bertani broth and induced for 16 to 20 hours at 18°C by the addition of 0.25 mM isopropyl-β-D-thiogalactopyranoside. An amount of target protein sufficient for the isolation of several milligrams of protein was present in the soluble fraction of the lysate from one liter of culture. Briefly, the cleared lysate in 20 mM tris-HCl (pH 8.0), 300 mM NaCl was applied to a nickel-nitrilotriacetic acid affinity column (QIAGEN) by gravity flow and eluted with successive buffers containing increasing amount of imidazole, followed by a polishing step by Superdex 200 (Cytiva) size exclusion chromatography (SEC). For crystallization, the 6xHis tag was removed with thrombin before the SEC step. The final purity was assessed to be >95% by SDS-PAGE, and the protein was concentrated to 8 to 10 mg/ml and stored at −80°C. All mutants were purchased from GenScript or obtained by standard site-directed mutagenesis techniques and confirmed by sequencing. All primers used were synthesized by Integrated DNA Technologies.

SPR studies on GSS binding to LMPTP

The Pioneer SensiQ system (currently Sartorius) was used in our SPR binding studies. The GSS protein was prepared in 10 mM sodium acetate buffer (pH 4.5) for immobilization by amine coupling. The protein was immobilized on channel 1 of the Octet SPR PCH Sensor Chip (Sartorius), while channel 2 was used as the reference channel. During immobilization, the Hepes-buffered saline, composed of 10 mM Hepes (pH 7.5) and 150 mM sodium chloride, was used as the running buffer. The immobilization was achieved by passing protein (2 μg/ml) over the sensor surface that was activated by the *N*-(3-dimethylaminopropyl)-*N*′-ethylcarbodiimide (EDC) and *N*-hydroxysuccinimide (NHS) reagents, and the sensor surface was subsequently deactivated by ethanolamine. The reference channel was activated by EDC and NHS, followed by deactivation using ethanolamine. Subsequently, the OneStep binding kinetics experiments were carried out using the running buffer (assay buffer) composed of 1X tris-buffered saline comprising 50 mM tris (pH 7.5), 150 mM sodium chloride, and 0.005% Tween 20. The analytes including 40 μM LMPTP and 80 μM HMG-box protein were prepared in the assay buffer and assessed for their binding to GSS. The HMG-box protein was used as a negative control. A bulk standard cycle (as an internal control for gradient dispersion) of 3% (w/w) sucrose prepared in the assay buffer, and few blank cycles of assay buffer were also included in the assay. The injection parameters for all the kinetics assay cycles include: flow rate of 40 μl/min, 100% of loop sample volume, and 360-min dissociation time. The data were processed using the Qdat analysis software.

GSS enzymatic assay

GSS activity assays were performed in reaction buffer containing 50 mM NaCl, 50 mM Hepes (pH 7.0), 10 mM $MgSO_4$, 10 mM glycine, 2 mM γ-glutamylcysteine, 2 mM dithiothreitol (DTT), and 0.05% Tween 20. GSS proteins were diluted in 1X reaction buffer to 20 nM. ATP was diluted in 1X reaction buffer to 2 mM. To a 384-well plate, 5 μl of 2 mM ATP in reaction buffer and 5 μl of 20 nM GSS in reaction buffer were added and incubated at 37°C for 30 min. Reactions were stopped with 10 μl ADP-Glo reagent from the ADP-Glo Kinase Assay kit (Promega, #V6930). Plates were incubated at room temperature away from light for 40 min. After incubation, 20 μl of Kinase Detection reagent (Promega, #V6930) was added and incubated at room temperature away from light for 1 hour. Bioluminescence was measured using the Tecan Infinite F Plex plate reader following incubation.

Crystallization and structure solution of GSS $Tyr^{270}Glu$

GSS $Tyr^{270}Glu$ was crystallized at 6 mg/ml in the presence of an equimolar amount of LMPTP by the hanging drop vapor diffusion method with 100 mM Hepes, 2.0 M ammonium sulfate, and 2% polyethylene glycol 400 (pH 7.5) as the reservoir buffer. A single crystal suitable for x-ray data collection grew over 2 to 4 months to a size of approximately 0.3 μm by 0.3 μm by 0.3 μm. The crystal was harvested and flash-frozen in liquid nitrogen with 25% glycerol as cryoprotectant, and a complete dataset to 1.5 Å resolution was collected at Beamline 8.2.1 of the Advanced Light Source (ALS) at Lawrence Berkeley National Laboratory. The data were processed with XDS (*62*) to a resolution of 1.59 Å based on a I/σI 2.0 cutoff. The structure was solved by molecular replacement using Phaser (*63*) and PDB code 2HGS as the search model and refined with Refmac5 (*64*) with model building with Coot (*65*). The final model comprises residues 3 to 474 and 5 to 474 for monomers A and B present in the asymmetric unit, with gaps at residues 368 to 371 and 455 to 463 (A) and 134 to 136, 368 to 370, and 456 to 459 (B), six sulfate ions; 1 glycerol molecule; and 1046 water molecules. Data collection and refinement statistics are reported in table S1. Structure quality was analyzed with Rampage (*66*). A detail of the ED map around the active site is shown in fig. S8B. Data and coordinates have been deposited in the PDB with accession code 8FBZ.

ROS detection assay

WT and LMPTP KO MyC-CaP cells were treated with 2.5 nM docetaxel or 1.5 nM cabazitaxel for 4 hours before harvesting. A ROS detection assay was performed using the DCFDA/H2DCFDA-Cellular ROS Assay kit (Abcam, #ab113851) following the manufacturer's instructions. Samples were analyzed in triplicate on black round bottom plates, and fluorescence intensity was measured at excitation = 485 and emission = 535 nm.

Cell apoptosis assay

WT and LMPTP KO MyC-CaP cells were seeded into a six-well plate in 10% FBS media. After 2 days, the cells were trypsinized and collected in the original cell media. The cells were washed with PBS and suspended in 100 μl of annexin V binding buffer before staining with 5 μl of Pacific Blue annexin V solution and 5 μl of propidium iodide solution (BioLegend). After incubating in the dark at room temperature for 15 min, 400 μl of annexin binding buffer was added to each sample. Samples were analyzed for cell fluorescence by flow cytometry using a Bio-Rad ZE5 flow cytometer, and the data were processed using FlowJo software.

Cell cycle phase determination

WT and LMPTP KO MyC-CaP cells (10^5 cells) were seeded into a six-well plate to attach overnight. The following day, cells were collected by trypsinization and prepared for cell cycle analysis by flow cytometry according to specifications of the Cell Cycle Phase Determination Kit (Cayman Chemical, #10009349). Cell fluorescence was measured using a BD LSR-II, and the data were processed according to the Dean-Jett-Fox model using the Cell Cycle tool from FlowJo software. Peak constraints were added only when necessary for the model to calculate cell cycle phases.

Statistical analysis

The one-way analysis of variance (ANOVA), two-way ANOVA, log-rank test, unpaired *t* test, unpaired *t* test with Welch's correction, and Mann-Whitney *U* test were performed using GraphPad Prism software. Statistical outliers were identified using the Grubbs test ($\alpha = 0.05$) in GraphPad Prism. *P* values less than 0.05 were considered significant. Statistical analysis of data from TCGA was reported by the UALCAN portal. Comparison of *ACP1* expression in various normal or tumor samples had been analyzed with a *t* test performed using a PERL script with Comprehensive Perl Archive Network module "Statistics::TTest" (*50*). Statistical significance of survival correlation between low-medium and high *ACP1* expression groups had been analyzed using a log-rank test (*50*). Differential *ACP1* gene expression in the Caris Life Sciences cohort was assessed by Mann-Whitney *U* tests for samples stratified by primary (prostate), lymph node, and metastatic biopsy sites. For the phosphoproteomics analysis, *P* values for phosphopeptide ratios were calculated by two-tailed *t* test and adjusted *P* values for each pathway were obtained using the Benjamini-Hochberg method in IPA.

Supplementary Materials

This PDF file includes:

Figs. S1 to S10
Table S1
Legends for data S1 to S12

Other Supplementary Material for this manuscript includes the following:

Data S1 to S12

REFERENCES AND NOTES

1. T. Karantanos, P. G. Corn, T. C. Thompson, Prostate cancer progression after androgen deprivation therapy: Mechanisms of castrate resistance and novel therapeutic approaches. *Oncogene* **32**, 5501–5511 (2013).
2. R. L. Siegel, K. D. Miller, A. Jemal, Cancer statistics, 2019. *CA Cancer J. Clin.* **69**, 7–34 (2019).
3. G. Pignot, D. Maillet, E. Gross, P. Barthelemy, J.-B. Beauval, F. Constans-Schlurmann, Y. Loriot, G. Ploussard, P. Sargos, M.-O. Timsit, S. Vincendeau, G. Pasticier, D. Borchiellini, Systemic treatments for high-risk localized prostate cancer. *Nat. Rev. Urol.* **15**, 498–510 (2018).
4. G. Oster, L. Lamerato, A. G. Glass, K. E. Richert-Boe, A. Lopez, K. Chung, A. Richhariya, T. Dodge, G. G. Wolff, A. Balakumaran, J. Edelsberg, Natural history of skeletal-related events in patients with breast, lung, or prostate cancer and metastases to bone: A 15-year study in two large US health systems. *Support. Care Cancer* **21**, 3279–3286 (2013).
5. C. Logothetis, M. J. Morris, R. Den, R. E. Coleman, Current perspectives on bone metastases in castrate-resistant prostate cancer. *Cancer Metastasis Rev.* **37**, 189–196 (2018).
6. J. P. Vainonen, M. Momeny, J. Westermarck, Druggable cancer phosphatases. *Sci. Transl. Med.* **13**, (2021).
7. L. L. Shekels, A. J. Smith, R. L. Van Etten, D. A. Bernlohr, Identification of the adipocyte acid phosphatase as a PAO-sensitive tyrosyl phosphatase. *Protein Sci.* **1**, 710–721 (1992).
8. F. Magherini, E. Giannoni, G. Raugei, P. Cirri, P. Paoli, A. Modesti, G. Camici, G. Ramponi, Cloning of murine low molecular weight phosphotyrosine protein phosphatase cDNA: Identification of a new isoform. *FEBS Lett.* **437**, 263–266 (1998).
9. G. Raugei, G. Ramponi, P. Chiarugi, Low molecular weight protein tyrosine phosphatases: Small, but smart. *Cell. Mol. Life Sci.* **59**, 941–949 (2002).
10. A. Alonso, J. Sasin, N. Bottini, I. Friedberg, I. Friedberg, A. Osterman, A. Godzik, T. Hunter, J. Dixon, T. Mustelin, Protein tyrosine phosphatases in the human genome. *Cell* **117**, 699–711 (2004).
11. A. Alonso, R. Pulido, The extended human PTPome: A growing tyrosine phosphatase family. *FEBS J.* **283**, 1404–1429 (2016).
12. A. Caselli, P. Paoli, A. Santi, C. Mugnaioni, A. Toti, G. Camici, P. Cirri, Low molecular weight protein tyrosine phosphatase: Multifaceted functions of an evolutionarily conserved enzyme. *Biochim. Biophys. Acta* **1864**, 1339–1355 (2016).
13. S. K. Pandey, X. X. Yu, L. M. Watts, M. D. Michael, K. W. Sloop, A. R. Rivard, T. A. Leedom, V. P. Manchem, L. Samadzadeh, R. A. McKay, B. P. Monia, S. Bhanot, Reduction of low molecular weight protein-tyrosine phosphatase expression improves hyperglycemia and insulin sensitivity in obese mice. *J. Biol. Chem.* **282**, 14291–14299 (2007).
14. S. M. Stanford, A. E. Aleshin, V. Zhang, R. J. Ardecky, M. P. Hedrick, J. Zou, S. R. Ganji, M. R. Bliss, F. Yamamoto, A. A. Bobkov, J. Kiselar, Y. Liu, G. W. Cadwell, S. Khare, J. Yu, A. Barquilla, T. D. Y. Chung, T. Mustelin, S. Schenk, L. A. Bankston, R. C. Liddington, A. B. Pinkerton, N. Bottini, Diabetes reversal by inhibition of the low-molecular-weight tyrosine phosphatase. *Nat. Chem. Biol.* **13**, 624–632 (2017).
15. S. M. Stanford, M. A. Diaz, R. J. Ardecky, J. Zou, T. Roosild, Z. J. Holmes, T. P. Nguyen, M. P. Hedrick, S. Rodiles, A. Guan, S. Grotegut, E. Santelli, T. D. Y. Chung, M. R. Jackson, N. Bottini, A. B. Pinkerton, Discovery of orally bioavailable purine-based inhibitors of the low-molecular-weight protein tyrosine phosphatase. *J. Med. Chem.* **64**, 5645–5653 (2021).
16. S. M. Stanford, M. Collins, M. A. Diaz, Z. J. Holmes, P. Gries, M. R. Bliss, A. Lodi, V. Zhang, S. Tiziani, N. Bottini, The low molecular weight protein tyrosine phosphatase promotes adipogenesis and subcutaneous adipocyte hypertrophy. *J. Cell. Physiol.* **236**, 6630–6642 (2021).
17. M. Ohtaka, Y. Miyoshi, T. Kawahara, S. Ohtake, M. Yasui, K. Uemura, S. Yoneyama, Y. Hattori, J.-I. Teranishi, Y. Yokomizo, H. Uemura, H. Miyamoto, M. Yao, Low-molecular-weight protein tyrosine phosphatase expression as a prognostic factor for men with metastatic hormone-naïve prostate cancer. *Urol. Oncol.* **35**, 607.e9–607.e14 (2017).
18. R. R. Ruela-de-Sousa, E. Hoekstra, A. M. Hoogland, K. C. Souza Queiroz, M. P. Peppelenbosch, A. P. Stubbs, K. Pelizzaro-Rocha, G. van Leenders, G. Jenster, H. Aoyama, C. V. Ferreira, G. M. Fuhler, Low-molecular-weight protein tyrosine phosphatase predicts prostate cancer outcome by increasing the metastatic potential. *Eur. Urol.* **69**, 710–719 (2016).
19. H. Kurose, K. Ueda, R. Kondo, S. Ogasawara, H. Kusano, S. Sanada, Y. Naito, J. Akiba, T. Kakuma, T. Igawa, H. Yano, Low-molecular-weight protein tyrosine phosphatase is a possible biomarker for predicting postoperative biochemical recurrence in prostate cancer with negative surgical margins. *Anticancer Res.* **39**, 957–964 (2019).
20. E. Hoekstra, L. L. Kodach, A. M. Das, R. R. Ruela-de-Sousa, C. V. Ferreira, J. C. Hardwick, C. J. van der Woude, M. P. Peppelenbosch, T. L. Ten Hagen, G. M. Fuhler, Low molecular weight protein tyrosine phosphatase (LMWPTP) upregulation mediates malignant potential in colorectal cancer. *Oncotarget* **6**, 8300–8312 (2015).
21. A. V. S. Faria, E. M. B. Fonseca, P. S. Fernandes-Oliveira, T. I. de Lima, S. P. Clerici, G. Z. Justo, L. R. Silveira, N. Duran, C. V. Ferreira-Halder, Violacein switches off low molecular weight tyrosine phosphatase and rewires mitochondria in colorectal cancer cells. *Bioorg. Chem.* **127**, 106000 (2022).
22. A. V. S. Faria, B. Yu, M. Mommersteeg, P. F. de Souza-Oliveira, S. S. Andrade, M. C. W. Spaander, M. P. M. de Maat, M. P. Peppelenbosch, C. V. Ferreira-Halder, G. M. Fuhler, Platelet-dependent signaling and low molecular weight protein tyrosine phosphatase expression promote aggressive phenotypic changes in gastrointestinal cancer cells. *Biochim. Biophys. Acta Mol. Basis Dis.* **1868**, 166280 (2022).
23. G. Lori, P. Paoli, A. P. Femia, E. Pranzini, A. Caselli, K. Tortora, A. Romagnoli, G. Raugei, G. Caderni, Morin-dependent inhibition of low molecular weight protein tyrosine phosphatase (LMW-PTP) restores sensitivity to apoptosis during colon carcinogenesis:

Studies in vitro and in vivo, in an Apc-driven model of colon cancer. *Mol. Carcinog.* **58**, 686–698 (2019).
24. R. Marzocchini, F. Malentacchi, M. Biagini, D. Cirelli, C. Luceri, G. Caderni, G. Raugei, The expression of low molecular weight protein tyrosine phosphatase is up-regulated in 1,2-dimethylhydrazine-induced colon tumours in rats. *Int. J. Cancer* **122**, 1675–1678 (2008).
25. D. G. Bostwick, Grading prostate cancer. *Am. J. Clin. Pathol.* **102**, S38–S56 (1994).
26. S. You, B. S. Knudsen, N. Erho, M. Alshalalfa, M. Takhar, H. Al-Deen Ashab, E. Davicioni, R. J. Karnes, E. A. Klein, R. B. Den, A. E. Ross, E. M. Schaeffer, I. P. Garraway, J. Kim, M. R. Freeman, Integrated classification of prostate cancer reveals a novel luminal subtype with poor outcome. *Cancer Res.* **76**, 4948–4958 (2016).
27. A. O. Elmehrath, A. M. Afifi, M. J. Al-Husseini, A. M. Saad, N. Wilson, K. S. Shohdy, P. Pilie, M. B. Sonbol, O. Alhalabi, Causes of death among patients with metastatic prostate cancer in the US from 2000 to 2016. *JAMA Netw. Open* **4**, e2119568 (2021).
28. E. Svensson, C. F. Christiansen, S. P. Ulrichsen, M. R. Rørth, H. T. Sørensen, Survival after bone metastasis by primary cancer type: A Danish population-based cohort study. *BMJ Open* **7**, e016022 (2017).
29. C. Paindelli, N. Navone, C. J. Logothetis, P. Friedl, E. Dondossola, Engineered bone for probing organotypic growth and therapy response of prostate cancer tumoroids in vitro. *Biomaterials* **197**, 296–304 (2019).
30. C. Paindelli, S. Casarin, F. Wang, L. Diaz-Gomez, J. Zhang, A. G. Mikos, C. J. Logothetis, P. Friedl, E. Dondossola, Enhancing ^{223}Ra treatment efficacy by anti-β1 integrin targeting. *J. Nucl. Med.* **63**, 1039–1045 (2022).
31. T. Bello, C. Paindelli, L. A. Diaz-Gomez, A. Melchiorri, A. G. Mikos, P. S. Nelson, E. Dondossola, T. S. Gujral, Computational modeling identifies multitargeted kinase inhibitors as effective therapies for metastatic, castration-resistant prostate cancer. *Proc. Natl. Acad. Sci. U.S.A.* **118**, (2021).
32. B. J. Altman, Z. E. Stine, C. V. Dang, From Krebs to clinic: Glutamine metabolism to cancer therapy. *Nat. Rev. Cancer* **16**, 619–634 (2016).
33. S. C. Lu, Glutathione synthesis. *Biochim. Biophys. Acta* **1830**, 3143–3153 (2013).
34. R. Gosu, S. M. Zaheer, in *Methods for Fragments Screening Using Surface Plasmon Resonance*, S. M. Zaheer, R. Gosu, Eds. (Springer Singapore, Singapore, 2021), pp. 5–7.
35. C. Alvarado, E. Stahl, K. Koessel, A. Rivera, B. R. Cherry, S. Pulavarti, T. Szyperski, W. Cance, T. Marlowe, Development of a fragment-based screening assay for the focal adhesion targeting domain using SPR and NMR. *Molecules* **24**, 3352 (2019).
36. G. Polekhina, P. G. Board, R. R. Gali, J. Rossjohn, M. W. Parker, Molecular basis of glutathione synthetase deficiency and a rare gene permutation event. *EMBO J.* **18**, 3204–3213 (1999).
37. V. P. Wellner, M. E. Anderson, R. N. Puri, G. L. Jensen, A. Meister, Radioprotection by glutathione ester: Transport of glutathione ester into human lymphoid cells and fibroblasts. *Proc. Natl. Acad. Sci. U.S.A.* **81**, 4732–4735 (1984).
38. K. Pakos-Zebrucka, I. Koryga, K. Mnich, M. Ljujic, A. Samali, A. M. Gorman, The integrated stress response. *EMBO Rep.* **17**, 1374–1395 (2016).
39. C. Sarcinelli, H. Dragic, M. Piecyk, V. Barbet, C. Duret, A. Barthelaix, C. Ferraro-Peyret, J. Fauvre, T. Renno, C. Chaveroux, S. N. Manié, ATF4-dependent *NRF2* transcriptional regulation promotes antioxidant protection during endoplasmic reticulum stress. *Cancers (Basel)* **12**, 569 (2020).
40. U. S. Srinivas, B. W. Q. Tan, B. A. Vellayappan, A. D. Jeyasekharan, ROS and the DNA damage response in cancer. *Redox Biol.* **25**, 101084 (2019).
41. T. Kosaka, H. Hongo, Y. Miyazaki, K. Nishimoto, A. Miyajima, M. Oya, Reactive oxygen species induction by cabazitaxel through inhibiting Sestrin-3 in castration resistant prostate cancer. *Oncotarget* **8**, 87675–87683 (2017).
42. D. Cao, B. Qiao, Z. Ge, Y. Yuan, Amplification loop cascade for increasing caspase activity induced by docetaxel. *J. Cell. Biochem.* **96**, 810–820 (2005).
43. O. S. Chao, O. B. Goodman Jr., DNA-PKc inhibition overcomes taxane resistance by promoting taxane-induced DNA damage in prostate cancer cells. *Prostate* **81**, 1032–1048 (2021).
44. B. L. Ingle, B. Shrestha, M. C. De Jesus, H. M. Conrad-Webb, M. E. Anderson, T. R. Cundari, Genetic mutations in the S-loop of human glutathione synthetase: Links between substrate binding, active site structure and allostery. *Comput. Struct. Biotechnol. J.* **17**, 31–38 (2019).
45. N. Dahl, M. Pigg, E. Ristoff, R. Gali, B. Carlsson, B. Mannervik, A. Larsson, P. Board, Missense mutations in the human glutathione synthetase gene result in severe metabolic acidosis, 5-oxoprolinuria, hemolytic anemia and neurological dysfunction. *Hum. Mol. Genet.* **6**, 1147–1152 (1997).
46. E. Ristoff, E. Mayatepek, A. Larsson, Long-term clinical outcome in patients with glutathione synthetase deficiency. *J. Pediatr.* **139**, 79–84 (2001).
47. L. Kennedy, J. K. Sandhu, M. E. Harper, M. Cuperlovic-Culf, Role of glutathione in cancer: From mechanisms to therapies. *Biomolecules* **10**, 1429 (2020).
48. T. S. de Souza Malaspina, W. F. Zambuzzi, C. X. dos Santos, A. P. Campanelli, F. R. Laurindo, M. C. Sogayar, J. M. Granjeiro, A possible mechanism of low molecular weight protein tyrosine phosphatase (LMW-PTP) activity modulation by glutathione action during human osteoblast differentiation. *Arch. Oral Biol.* **54**, 642–650 (2009).
49. K. Xing, A. Raza, S. Löfgren, M. R. Fernando, Y.-S. Ho, M. F. Lou, Low molecular weight protein tyrosine phosphatase (LMW-PTP) and its possible physiological functions of redox signaling in the eye lens. *Biochim. Biophys. Acta* **1774**, 545–555 (2007).
50. D. S. Chandrashekar, B. Bashel, S. A. H. Balasubramanya, C. J. Creighton, I. Ponce-Rodriguez, B. Chakravarthi, S. Varambally, UALCAN: A portal for facilitating tumor subgroup gene expression and survival analyses. *Neoplasia* **19**, 649–658 (2017).
51. M. J. Goldman, B. Craft, M. Hastie, K. Repecka, F. McDade, A. Kamath, A. Banerjee, Y. Luo, D. Rogers, A. N. Brooks, J. Zhu, D. Haussler, Visualizing and interpreting cancer genomics data via the Xena platform. *Nat. Biotechnol.* **38**, 675–678 (2020).
52. F. Wade, P. Quijada, K. M. Al-Haffar, S. M. Awad, M. Kunhi, H. Toko, Q. Marashly, K. Belhaj, I. Zahid, F. Al-Mohanna, S. M. Stanford, R. Alvarez, Y. Liu, D. Colak, M. C. Jordan, K. P. Roos, A. Assiri, W. Al-Habeeb, M. Sussman, N. Bottini, C. Poizat, Deletion of low molecular weight protein tyrosine phosphatase (Acp1) protects against stress-induced cardiomyopathy. *J. Pathol.* **237**, 482–494 (2015).
53. P. A. Watson, K. Ellwood-Yen, J. C. King, J. Wongvipat, M. M. Lebeau, C. L. Sawyers, Context-dependent hormone-refractory progression revealed through characterization of a novel murine prostate cancer cell line. *Cancer Res.* **65**, 11565–11571 (2005).
54. E. J. Adams, W. R. Karthaus, E. Hoover, D. Liu, A. Gruet, Z. Zhang, H. Cho, R. DiLoreto, S. Chhangawala, Y. Liu, P. A. Watson, E. Davicioni, A. Sboner, C. E. Barbieri, R. Bose, C. S. Leslie, C. L. Sawyers, FOXA1 mutations alter pioneering activity, differentiation and prostate cancer phenotypes. *Nature* **571**, 408–412 (2019).
55. C. A. Schneider, W. S. Rasband, K. W. Eliceiri, NIH Image to ImageJ: 25 years of image analysis. *Nat. Methods* **9**, 671–675 (2012).
56. J. K. Eng, M. R. Hoopmann, T. A. Jahan, J. D. Egertson, W. S. Noble, M. J. MacCoss, A deeper look into comet—Implementation and features. *J. Am. Soc. Mass Spectrom.* **26**, 1865–1874 (2015).
57. S. F. Rusin, M. E. Adamo, A. N. Kettenbach, Identification of candidate casein kinase 2 substrates in mitosis by quantitative phosphoproteomics. *Front. Cell Dev. Biol.* **5**, 97 (2017).
58. S. Thomas, D. Bonchev, A survey of current software for network analysis in molecular biology. *Hum. Genomics* **4**, 353–360 (2010).
59. X. Lu, G. L. Hackman, A. Saha, A. S. Rathore, M. Collins, C. Friedman, S. S. Yi, F. Matsuda, J. DiGiovanni, A. Lodi, Metabolomics-based phenotypic screens for evaluation of drug synergy via direct-infusion mass spectrometry. *Iscience* **25**, 104221 (2022).
60. R. Pandey, C. L. Riley, E. M. Mills, S. Tiziani, Highly sensitive and selective determination of redox states of coenzymes Q_9 and Q_{10} in mice tissues: Application of orbitrap mass spectrometry. *Anal. Chim. Acta* **1011**, 68–76 (2018).
61. D. S. Wishart, A. Guo, E. Oler, F. Wang, A. Anjum, H. Peters, R. Dizon, Z. Sayeeda, S. Tian, B. L. Lee, M. Berjanskii, R. Mah, M. Yamamoto, J. Jovel, C. Torres-Calzada, M. Hiebert-Giesbrecht, V. W. Lui, D. Varshavi, D. Varshavi, D. Allen, D. Arndt, N. Khetarpal, A. Sivakumaran, K. Harford, S. Sanford, K. Yee, X. Cao, Z. Budinski, J. Liigand, L. Zhang, J. Zheng, R. Mandal, N. Karu, M. Dambrova, H. B. Schiöth, R. Greiner, V. Gautam, HMDB 5.0: The human metabolome database for 2022. *Nucleic Acids Res.* **50**, D622–D631 (2022).
62. W. Kabsch, Xds., XDS. *Acta Crystallogr. D Biol. Crystallogr.* **66**, 125–132 (2010).
63. A. J. McCoy, R. W. Grosse-Kunstleve, P. D. Adams, M. D. Winn, L. C. Storoni, R. J. Read, Phaser crystallographic software. *J. Appl. Cryst.* **40**, 658–674 (2007).
64. G. N. Murshudov, A. A. Vagin, E. J. Dodson, Refinement of macromolecular structures by the maximum-likelihood method. *Acta Crystallogr. D Biol. Crystallogr.* **53**, 240–255 (1997).
65. P. Emsley, B. Lohkamp, W. G. Scott, K. Cowtan, Features and development of Coot. *Acta Crystallogr. D Biol. Crystallogr.* **66**, 486–501 (2010).
66. S. C. Lovell, I. W. Davis, W. B. Arendall III, P. I. de Bakker, J. M. Word, M. G. Prisant, J. S. Richardson, D. C. Richardson, Structure validation by Cα geometry: ϕ,ψ and Cβ deviation. *Proteins* **50**, 437–450 (2003).
67. E. F. Pettersen, T. D. Goddard, C. C. Huang, G. S. Couch, D. M. Greenblatt, E. C. Meng, T. E. Ferrin, UCSF Chimera—A visualization system for exploratory research and analysis. *J. Comput. Chem.* **25**, 1605–1612 (2004).

Acknowledgments: We thank C. L. Sawyers for providing the MyC-CaP and MyC-CaP/GFP-Luc cell lines. **Funding:** This work was supported by National Institutes of Health grants R01 DK106233 and R01 HL152717 to N.B. and R21 CA245621 to S.M.S. and A.N.K., University of Texas System (STAR Award) to S.T., and American Cancer Society Institutional Research Grant 15-172-45-IRG to S.M.S. provided through the University of California San Diego Moores Cancer Center, Department of Defense Prostate Cancer Research Program DoD award nos. W81XWH-18-2-0013, W81XWH-18-2-0015, W81XWH-18-2-0016, W81XWH-18-2-0017, W81XWH-18-2-0018, and W81XWH-18-2-0019 PCRP Prostate Cancer Biorepository Network (PCBN). The ALS-ENABLE beamlines are supported in part by the National Institutes of Health, National Institute of General Medical Sciences, grant P30 GM124169-01. The Advanced Light Source is a Department of Energy Office of Science User Facility under contract no. DE-AC02-05CH11231. **Author contributions:** Conceptualization: S.M.S. and N.B. Methodology: S.M.S., T.P.N., J.C., E.D., A.G.M., A.L., S.T., A.N.K., and N.B. Investigation: S.M.S., T.P.N., J.C., Z.Z., G.L.H., E.S., C.M.S., M.K., E.D., B.L.B., M.A.D., Y.Z., S.H.R., P.A.W., B.S., C.P., V.P., A.E., A.L., A.B., R.R.M., R.M., S.T., A.N.K., and N.B. Visualization: S.M.S., T.P.N., J.C., Z.Z., G.L.H., E.S., C.M.S., M.K., E.D., B.L.B.,

M.A.D., Y.Z., S.H.R., A.E., and R.M. Funding acquisition: S.M.S., S.T., A.N.K., and N.B. Project administration: S.M.S., T.P.N., J.C., R.R.M., and N.B. Supervision: S.M.S. and N.B. Writing—original draft: S.M.S., T.P.N., and N.B., Writing—review and editing: S.M.S., T.P.N., J.C., Z.Z., G.L.H., E.S., C.M.S., M.K., E.D., B.L.B., M.A.D., Y.Z., S.H.R., P.A.W., B.S., C.P., V.P., A.G.M., A.E., A.L., A.B., R.R.M., R.M., S.T., A.N.K., and N.B.. **Competing interests:** N.B. and S.M.S. have a relationship with Nerio Therapeutics, Inc. which consists of being scientific founders with stock options and acting as consultants with income. The terms of this arrangement have been reviewed and approved by the University of California, San Diego and Cedars-Sinai Medical Center in accordance with their conflict of interest policies. P.A.W. receives royalty payments for the MyC-CaP cell line from the University of California. R.R.M. serves on the advisory boards/as consultant for Aveo, AstraZeneca, Bayer, BMS, Calithera, Caris, Dendreon, Exelixis, JNJ, Myovant, Merck, Novartis, Pfizer, Sanofi, SeaGen, Sorrento Therapeutics, and Tempus and receives research funding from Bayer, AstraZeneca, and Tempus. **Data and materials availability:** All data needed to evaluate the conclusions in the paper are present in the paper and/or the Supplementary Materials. DNA sequences for plasmids used in this study can be found in the Supplementary Materials. The coordinates and diffraction data for the crystal structure described in this study have been deposited to the PDB (www.rcsb.org) with ID 8FBZ. We will release the atomic coordinates upon article publication. The phosphoproteomics data for this study have been deposited in the MassIVE database with ID MSV000092695 (https://massive.ucsd.edu/ProteoSAFe/dataset.jsp?task=991db262e095452cb1be7ca81cd2eae5). The MyC-CaP/GFP-Luc cell line can be provided by Memorial Sloan Kettering pending scientific review and a completed material transfer agreement. Requests should be submitted to C. L. Sawyers. Tissue samples from the PCBN can be provided based on availability and pending scientific review and a completed material transfer agreement. Requests should be submitted to querypcbn@lists.johnshopkins.edu. The deidentified data associated with Fig. 1 (D and H) are owned by Caris Life Sciences. Qualified researchers can apply for access to these summarized data by contacting A.E. at aelliott@carisls.com and signing a data usage agreement.

Submitted 20 January 2023
Accepted 29 December 2023
Published 31 January 2024
10.1126/sciadv.adg7887